

Lawrence Berkeley National Laboratory

LBL Publications

Title

Carbon Dioxide Plume Evolution Following Injection into a Depleted Natural Gas Reservoir:
Modeling of Conformance Uncertainty Reduction Over Time

Permalink

<https://escholarship.org/uc/item/1wv2q0ng>

Authors

Doughty, Christine
Oldenburg, Curtis

Publication Date

2019

Peer reviewed

1
2
3
4
5
6
7
8
9
10
11
12
13
14
15
16
17

Carbon Dioxide Plume Evolution Following Injection into a Depleted Natural Gas Reservoir:

Modeling of Conformance Uncertainty Reduction Over Time

Christine Doughty and Curtis M. Oldenburg

Earth and Environmental Sciences, Lawrence Berkeley National Laboratory

Berkeley, CA 94720 USA

August 15, 2019

Keywords: Geologic carbon sequestration; post-injection site care, uncertainty, conformance,
Class VI; depleted gas reservoir

18 **Abstract**

19 The uncertainty in the long-term fate of CO₂ injected for geologic carbon sequestration (GCS) is
20 a significant barrier to the adoption of GCS as a greenhouse gas emission mitigation approach
21 for industry and regulatory agencies alike. Here we present a modeling study that demonstrates
22 that the uncertainty in forecasts of GCS site performance decreases over time as monitoring data
23 are used to inform and update operational models. The approach we take is to consider a case
24 study consisting of a depleted natural gas reservoir that is used for GCS with CO₂ injection
25 occurring over 20 years, with a 50-year post-injection site care (PISC) period. We constructed a
26 detailed model of the system and ran this model out to 200 years to generate the *actual* site data.
27 A series of simpler *operational* models based on limited data and assumptions about how an
28 actual operator would model such a site are then run and compared against the actual model
29 output at various specific monitoring points after one year, two years, etc. The operational model
30 is then updated and improved using the observations (synthetic data from the actual model) at the
31 same time intervals. We found that both model parameter values and model features needed to be
32 added over time to improve matches to the actual system. These kinds of model adjustments are
33 expected to be a normal part of reservoir engineering and site management at GCS sites. We
34 found that the uncertainty in two key measures related to site performance at various locations
35 decreases with time. This overall conclusion should help allay the concerns of industry and
36 regulators about the uncertainty in GCS operations.

37 **1. Introduction**

38 In order to make a substantial impact in reducing greenhouse gas emissions, geologic carbon
39 sequestration (GCS) will need to involve injection of millions of tonnes of CO₂ at many sites
40 worldwide over several decades. Following injection there will be a post-injection site care

41 (PISC) period during which monitoring will be carried out so that the operator can ensure that
42 CO₂ storage is permanent and that the project is not impacting underground sources of drinking
43 water (USDW). The U.S. EPA in its Class VI CO₂ injection well permitting regulation specifies
44 50 years as a period over which monitoring should be carried out during PISC (EPA, 2008),
45 while the California Air Resources Board (2017) is currently suggesting a period of 100 years is
46 needed for monitoring to ensure permanence. Given the lack of experience with industrial-scale
47 CO₂ injection for GCS, the costs of multi-decadal monitoring operations during PISC are
48 difficult to forecast, and this uncertainty is increasing the estimated lifecycle cost of GCS. Given
49 the widespread agreement that GCS must be part of the solution for reducing effective
50 greenhouse gas emissions (IPCC, 2018), there is strong motivation to understand more about the
51 long-term evolution of injected CO₂ in the subsurface and the evolution of uncertainty in CO₂
52 storage as large-scale projects mature over time.

53 To address the above lack of knowledge, we have undertaken a modeling and simulation study
54 that makes use of a synthetic GCS project about which everything is known by virtue of detailed
55 numerical simulations. However, in this approach we assume that our knowledge of the GCS
56 project is limited to model results that represent observations made at a limited number of
57 monitoring wells, for a limited period of time. This limited information is used to develop a
58 series of operational model of the GCS project, whose long-term predictions for CO₂ plume
59 evolution are then compared with those of the detailed model representing the actual system. In
60 this study, this procedure is repeated periodically, with more synthetic data becoming available
61 as time progresses. The idea is that by examining synthetic monitoring data from the virtual
62 GCS project at a series of times, we can determine how operational models improve over time as
63 more data become available, and thereby reduce forecast uncertainty over time. With this

64 understanding of uncertainty evolution in hand, we can make recommendations about how much
65 uncertainty there is in typical model-based forecasts of CO₂ plume and pressure evolution and
66 how uncertainty evolves over time for the given injection scenario.

67 The example studied here considers a depleted natural gas reservoir system typical of large GCS
68 opportunities in the Sacramento River Delta region of California. It was previously suggested
69 that depleted gas reservoirs are, by virtue of their proven capacity to store a buoyant gas (i.e.,
70 methane), low-hanging fruit for large-scale GCS (Oldenburg et al., 2001). The objective of this
71 study is to demonstrate the reduction in uncertainty over time of forecasts of plume properties as
72 the updated operational models incorporate more field observational data and become more
73 detailed and skilled at forecasting over time. We will show that not only does the uncertainty in
74 forecasts of plume extent and pressure rise decrease, but so too will associated estimates of risk.
75 The overall impact of these findings may have bearing on the time periods required for PISC. In
76 addition, our study informs the needed monitoring intensity and related costs which also may be
77 confidently estimated to decline with time based on our study. Finally, results of the study may
78 cause risk-averse stakeholders to gain tolerance for uncertainty in early forecasts of a GCS
79 project, knowing uncertainty will diminish over time.

80 **2. Background**

81 A survey of the literature on uncertainty reduction in GCS and other hydrologic systems
82 uncovers a large body of research based on sophisticated approaches such as modified Kalman
83 filters (Chen and Zhang, 2006; Sun et al., 2009), enhanced Monte Carlo methods (Keating et al.,
84 2010), and polynomial chaos expansion (Oladyshkin et al., 2011; Walter et al., 2012). Our study
85 does not utilize any sophisticated, elegant, or new techniques. The novelty is instead in the use of

86 a large synthetic system as a proxy for a real system, and the application to GCS where there is
87 an urgent need for understanding of long-term evolution of model forecast uncertainty. Our study
88 is also novel in that we couch uncertainty reduction in forecasts of CO₂ storage risk in terms of
89 reduction in uncertainty of conformance.

90 In order to make the approach and findings of this study concise, it is useful to introduce the
91 concept of conformance, which combines concordance and performance (e.g., Chadwick and
92 Noy, 2015; Oldenburg, 2018). In the GCS context, concordance is the degree to which model
93 forecasts of plume extent, pressure rise, etc. match observations, and performance is the degree
94 to which the storage system is performing as designed. For example, models should be able to
95 history-match observations (known in some fields as hindcasting), and the monitoring system
96 should be indicating that CO₂ is filling the intended storage reservoir, not leaking, not impacting
97 underground sources of drinking water (USDW), and not causing pressure rise above tolerable
98 ranges. If all of these conditions are met, we can say the system is conforming. In terms of
99 regulators and stakeholders, a conforming GCS project is a successful GCS project.

100 Nevertheless, as with all subsurface technologies, there is uncertainty involved in the assessment
101 of conformance, and this uncertainty must be understood in order to understand the robustness of
102 conformance assessment (e.g., Harp et al., 2019).

103 Further to the above, we address in this study the reduction in uncertainty in forecasts of
104 conformance. Conformance forecasts are uncertain because the underlying model predictions are
105 uncertain. In the present study, we use synthetic system performance data to quantify the
106 uncertainty in operational model forecasts and make conclusions about how that uncertainty
107 diminishes over time in a project as the operational model improves as experience with the
108 system is accumulated. Therefore, this study addresses the question of the reduction in

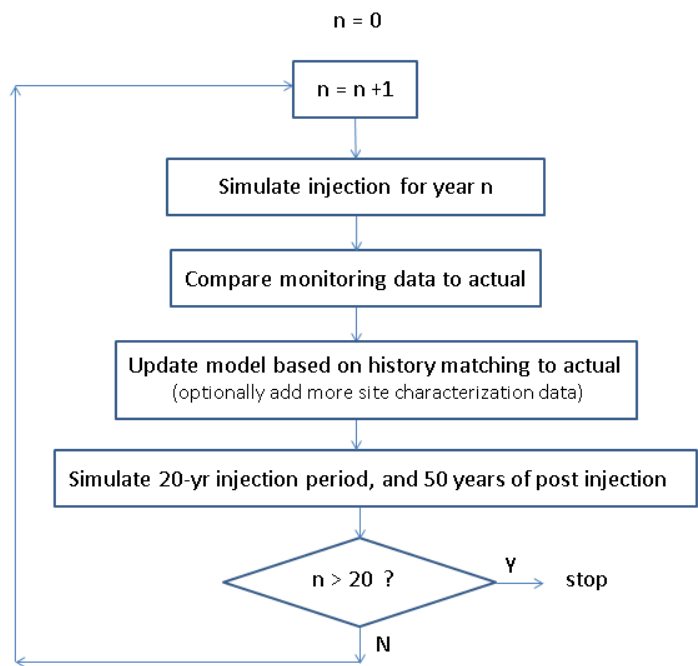
109 uncertainty (during GCS operations as models are improved) of forecasts of conformance.
110 Additional uncertainty enters into conformance assessments from the incomplete knowledge
111 arising from imprecise monitoring observations. We have not included this aspect into the study
112 in order to focus attention on the uncertainty that diminishes as experience with a system is
113 gained over time and as that experience is incorporated into operational models.

114 **3. Approach**

115 The approach we take involves use of a detailed model of a GCS scenario at a site to generate a
116 set of synthetic data that constitute the *actual* system. This actual system includes several
117 monitoring wells from which discrete observational data are assumed to be known from
118 monitoring. We assume that the operators of the project would have an *operational* model of the
119 CO₂ injection and storage system that they use for injection design, risk assessment, monitoring
120 design, and permitting. Assuming the project is permitted and injection begins, observations and
121 performance data would be used to update the operational model. This study carries out this
122 observation-model update loop to demonstrate the reduction in uncertainty of model forecasts
123 over time. The procedure is outlined in flow chart form in Figure 1 where the CO₂ injection
124 period is 20 years and the PISC period is assumed to be 50 years following the U.S. EPA Class
125 VI regulation (U.S. EPA, 2008).

126 We first define an injection scenario and design a logical and practical monitoring program. We
127 then create a detailed numerical model and simulate 20 years of large-scale CO₂ injection and
128 180 years of shut-in to create a synthetic “actual” case of performance and monitoring data. This
129 synthetic data set is then set aside. Using a subset of characterization data, we then create a
130 simplified operational model conceived as being similar to one that an actual operator would

131 develop based on available data, which are assumed to be much more limited than the data that
132 went into defining the actual model. As shown in the flowchart of Figure 1, we use the
133 operational model to simulate injection and monitoring for the first year. Based on a comparison
134 of operational model monitoring observations to actual model monitoring observations (assumed
135 to be 100% correct, i.e., no measurement uncertainty) at discrete monitoring well locations at the
136 end of Year 1, we then adjust the simplified operational model (history match) and make a
137 forecast for Year 2. We then repeat this process over the years of injection (see Figure 1). We
138 demonstrate by this approach that the simplified operational model becomes better and better
139 over time (uncertainty decreases) in making long-term forecasts, as observations are incorporated
140 into the model to improve its annual forecasting skill.



141

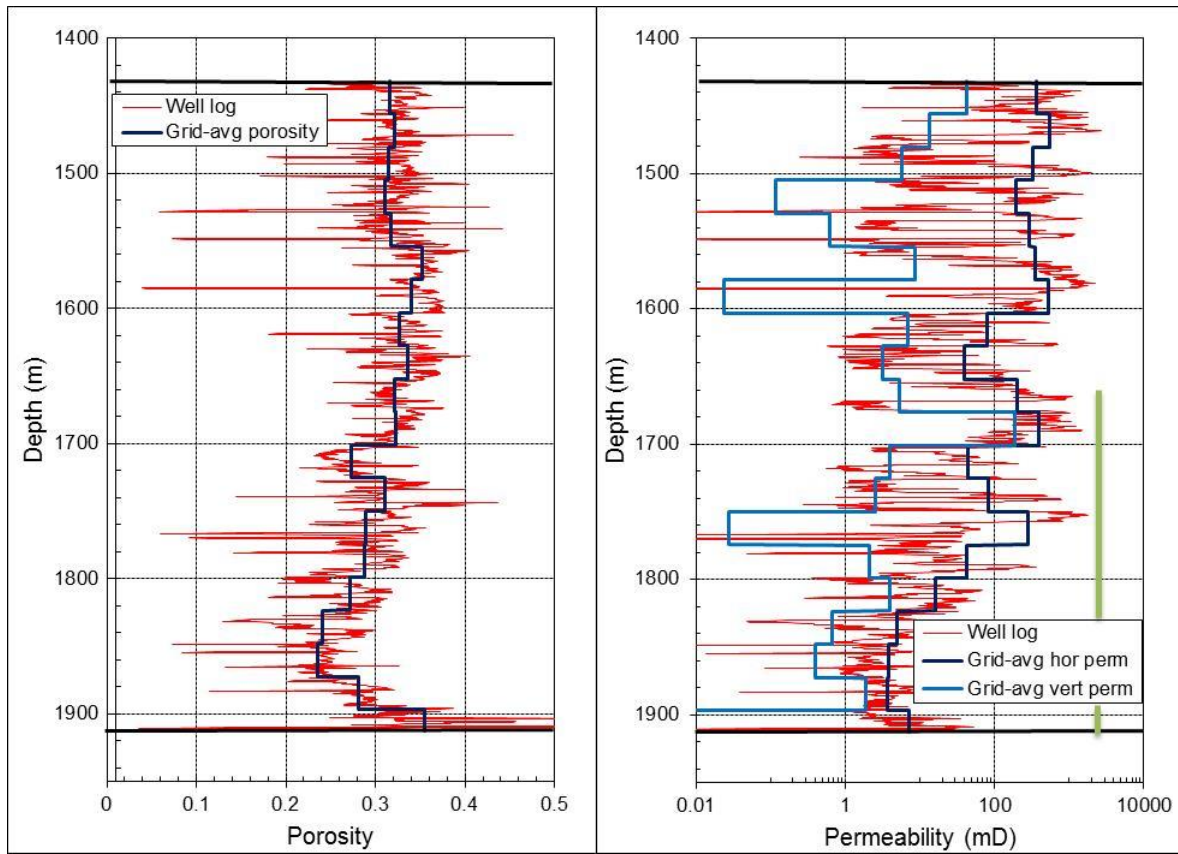
142 *Figure 1. Flow chart showing the updating and forward simulation steps for the operational*
143 *model used in the study.*

144

145 **Actual Depleted Gas Reservoir System**

146 *California Delta Geologic Setting*

147 The simulated system we use as the actual model has properties based on a site that is
148 representative of typical large-scale depleted natural gas (CH₄) reservoirs in the Sacramento
149 River Delta area of California. This region in the southwestern Sacramento Valley is within 50
150 miles (80 km) of several San Francisco Bay Area refineries that may someday capture CO₂ for
151 GCS. An unpublished regional-scale geologic model (see Burton et al., 2016) provides the
152 overall geologic structure. The sandstone storage reservoir we consider has variable thickness
153 averaging approximately 500 m at depths of 1000-2000 m. The storage reservoir is composed of
154 high-permeability sandstone with local low-permeability zones; it is generally dipping at 1.6° to
155 the SW, and is capped by an impermeable shale over an undulating reservoir top surface.
156 Layering within the sandstone storage reservoir is based on a well log (Figure 2) from a
157 Sacramento River Delta well (Burton et al., 2016), and we add stochastic heterogeneity to each
158 model layer using GSLIB (Deutsch and Journel, 1992) (Figure 3). Two sub-vertical faults are
159 included that inhibit cross-flow, but enhance flow parallel to the faults. The depth of the top of
160 the storage formation is shown in Figure 4, revealing the dip and attic regions in the storage
161 reservoir. The brine in the system initially is assumed to contain dissolved CH₄, consistent with it
162 being a depleted gas reservoir. While many of the larger natural gas reservoirs in the Sacramento
163 River Delta area are depleted, free-phase CH₄ is often still present in localized attic regions
164 trapped up against the caprock (Figure 5) and we assume that is the case here. As shown below,
165 injected CO₂ buoyantly pinned in the upper-most regions of the storage reservoir will tend to
166 migrate NE toward the shallowest regions and into attics in the reservoir that contain residual
167 free-phase CH₄.

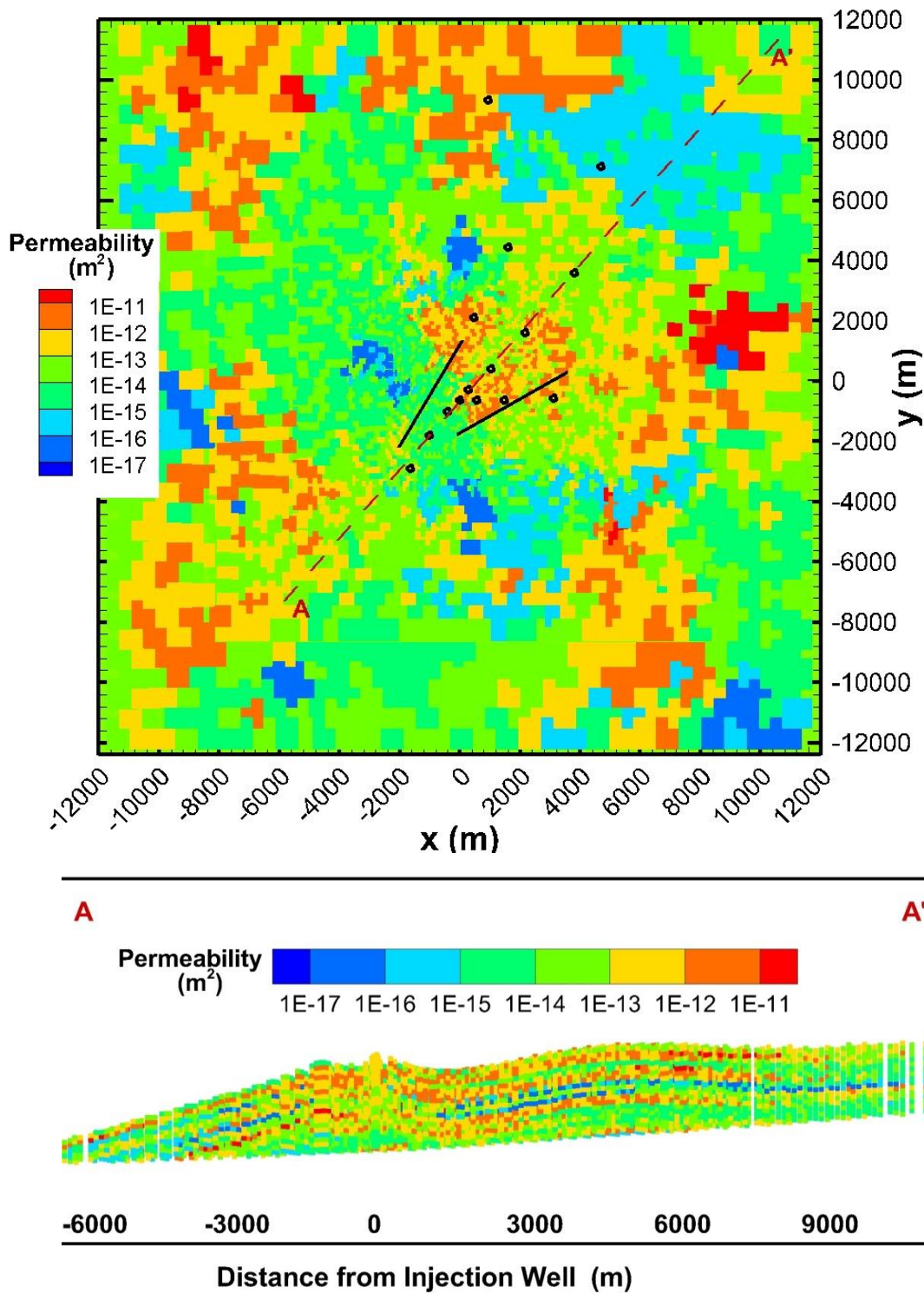


168

169

170

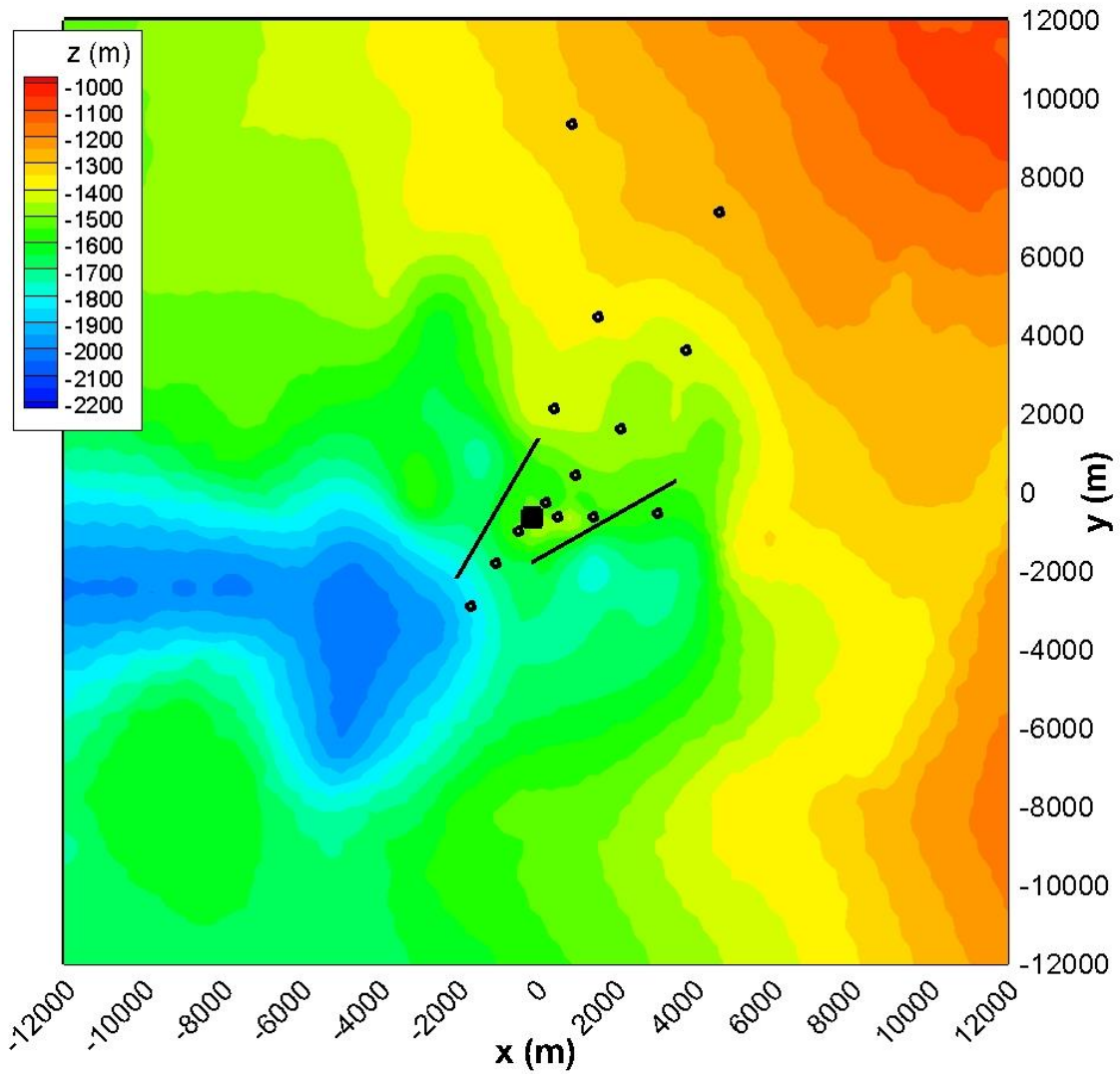
Figure 2. Well-log data used to determine layer porosities and permeabilities at the injection well in the actual model. The perforated interval is shown as a green bar.



171

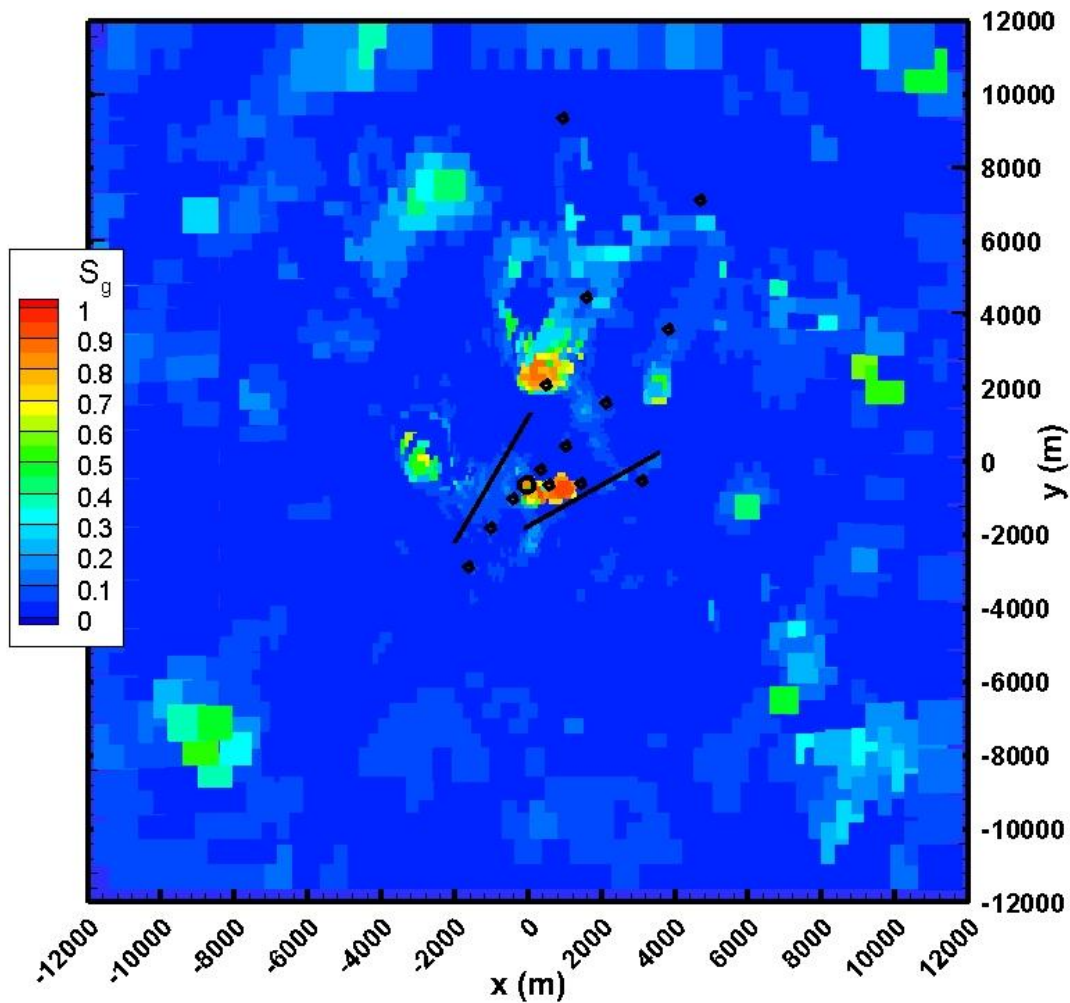
172

173 *Figure 3. (top) The center region of the top layer of the storage reservoir in the actual model,*
 174 *illustrating the heterogeneous permeability distribution along with monitoring wells (black*
 175 *circles). Two vertical faults are shown as black line segments. (bottom) Vertical cross-section at*
 176 *the location of the dashed line shown in the top frame showing the reservoir heterogeneity and*
 177 *locally closed structures (attics). Vertical exaggeration is two times.*



179
180

181 *Figure 4. Elevation of the top of the storage formation assuming ground surface is at $z = 0$ m.*
 182 *The injection well (black square) is NE of a deep pendant of the caprock (blue region). Buoyancy*
 183 *is expected to carry CO_2 to the NE toward the yellow and reddish colored attics of the reservoir.*



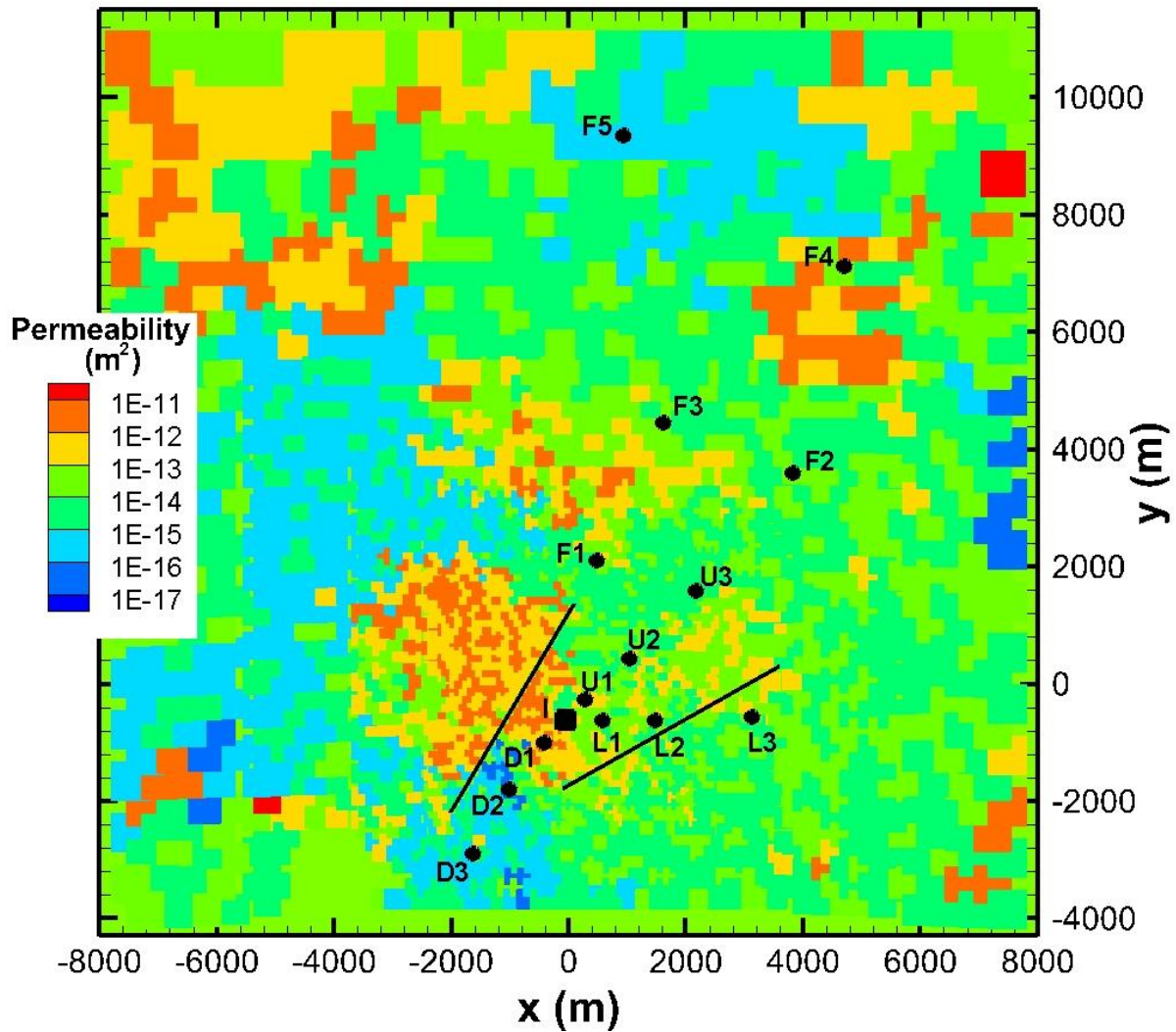
184
 185 *Figure 5. Initial saturation conditions in the actual model showing free-phase CH₄ localized in*
 186 *attic regions by buoyancy forces.*

187

188 ***Injection and Monitoring Scenario***

189 The scenario simulated specifies 8 Mt/yr of CO₂ injection for 20 years, and we run the
 190 simulation out another 180 years to observe very long-term evolution. Injection is into the lower
 191 half of the storage reservoir allowing for buoyant rise of injected CO₂ up into the attic regions of
 192 the reservoir. Studies such as Foxall et al. (2017) found that in highly permeable California Delta

193 sandstones, one well was sufficient to inject at this rate (i.e., near-well pressure remains below
194 frac pressure). The injection well and 14 monitoring wells are included in the model to serve as
195 points in the system where measurements of pressure, saturation, and gas composition are
196 assumed to be made over time (Figure 6). At the injection well (I) and at nine nearby monitoring
197 wells (D, L, U wells, named for their general locations downstream, lateral, and upstream
198 relative to the injection well), we assume monitoring is done at two depths: (1) top of the
199 perforated interval, and (2) top of the storage reservoir. At five more-distant wells (F wells,
200 named for being far from the injection well), we assume monitoring is done only at the top of the
201 storage reservoir. The total number of monitoring wells assumed here is probably unrealistically
202 large (i.e., more than would be installed in any actual project, especially in the early stages of
203 injection), but for this simulation study we need good spatial coverage to demonstrate how
204 pressure and saturation change in the system for the entire project period. While pressure is
205 assumed to be available continuously, saturation measurements (e.g., obtained using a pulsed
206 neutron logging technique such as Schlumberger's time-lapse Reservoir Saturation Tool (RST))
207 and fluid sampling to measure gas- and liquid-phase composition, e.g., by U-Tube sampling
208 (Freifeld et al., 2005), could be carried out at discrete times. Although not used for the present
209 study, continuous temperature measurements are straightforward to make, and would likely be
210 part of any monitoring dataset at GCS sites.



211

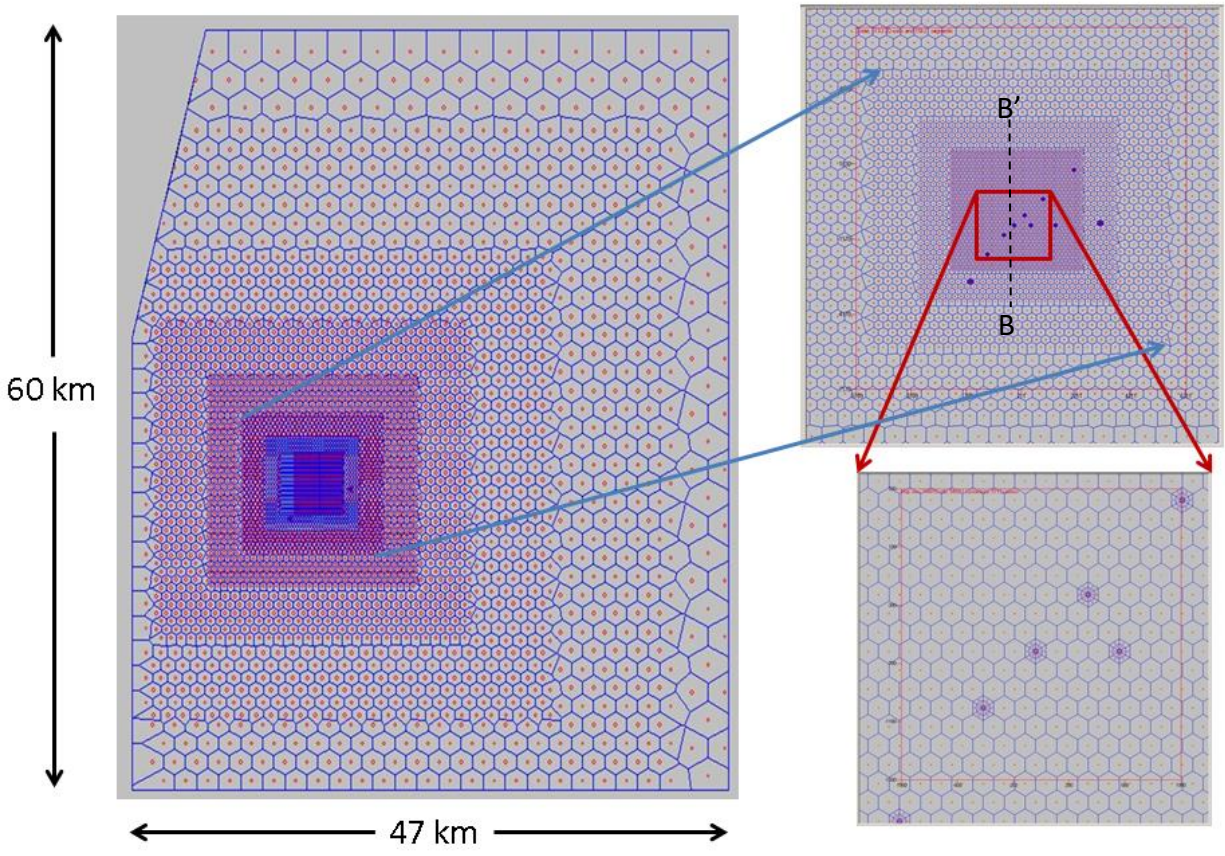
212 *Figure 6. The injection well (square) and monitoring well layout. The background shows the*
 213 *permeability distribution in the fourth layer of the reservoir in the actual model to illustrate the*
 214 *vertical variation compared to the top layer shown in Figure 3.*

215

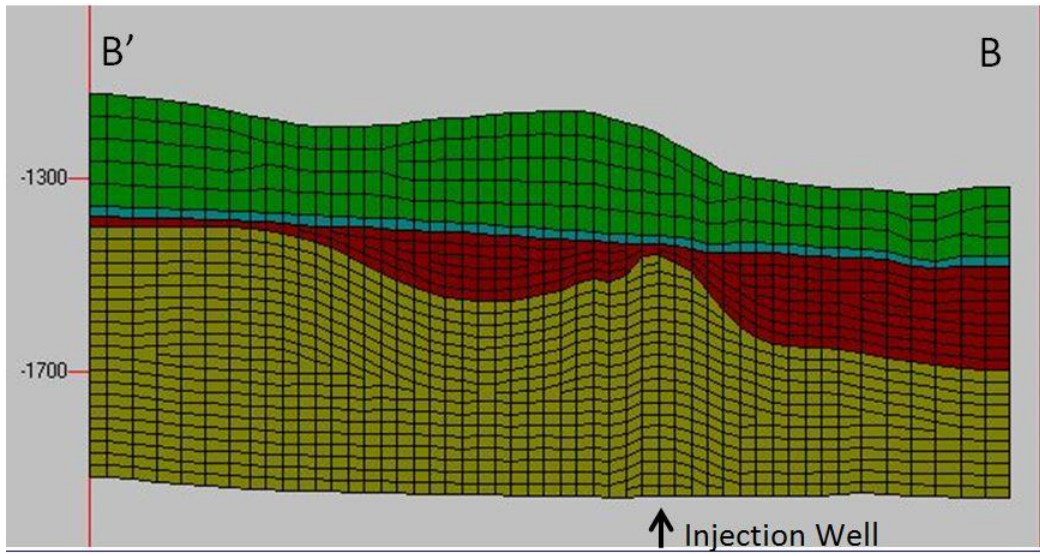
216 ***Domain Discretization***

217 In plan view, the model domain is 47 km by 60 km as shown in Figure 7. We discretized the
 218 domain finely around the injection and monitoring wells, and gradually coarsened the grid
 219 toward the boundaries. Hexagonal grid blocks are used to reduce grid-orientation effects. The

220 west and south boundaries are approximately aligned with regional faults that are assumed to be
221 impermeable to trans-fault flow. The east (right-hand side) boundary is up-dip and open to flow,
222 while the north boundary is closed. Vertical discretization (Figure 7) follows layers from the
223 geologic model (see Burton et al., 2016) with variable thickness layers that can pinch out. The
224 grid for the storage formation has 20 layers at the injection well, and 30 layers at its thickest
225 point.



226



227

228 *Figure 7. (top) Map view of 3D grid showing grid refinement around injection and monitoring*
 229 *wells that are roughly aligned with the expected plume migration path updip (see Figure 4);*
 230 *(bottom) N-S cross-section passing close to the injection well. Vertical exaggeration is five times.*
 231 *Yellow color shows the storage formation, red and blue are low-permeability seals, and green is*
 232 *an overlying aquifer.*

233

234 **Operational Model System**

235 It is important to remember that the model described above was created to generate the synthetic
236 data (i.e., describing the actual system) that will be compared to a series of subsequent models.

237 We will refer to the two classes of models as the actual model and the operational model,
238 respectively. The operational model is developed to mimic the kind of model that operators of
239 the site would use to design the injection scenario, design monitoring plans, estimate Area of
240 Review (AoR), obtain their injection permit(s), and manage ongoing operations. The first
241 operational model is based on data available prior to injection. Moreover, the first operational
242 model and its early updates may be developed based on subsets of all of the monitoring wells
243 that are ultimately installed (i.e., early operational models will be developed prior to all of the
244 wells being installed), again resulting in reliance on a limited set of data. In general, the
245 operational model will be simpler and more generalized early in a project and become more
246 detailed and accurate later in the project. The present study is aimed at demonstrating such
247 improvement and corresponding reduction in uncertainty of model results and forecasts.

248 The operational model utilizes the same grid and boundary conditions as the actual model. But
249 we assume that early in the project the operators would simplify the reservoir system and assume
250 it to be homogeneous. Furthermore, complexities like hysteresis in relative permeability and
251 capillary pressure would likely be omitted due to lack of data. Similarly the inclusion of residual
252 CH₄ in the system is a complication that would likely be left out for simplicity in early
253 operational models. In Table 1, we summarize the properties of the actual and operational
254 models. The years at which various features were added to the operational models are also
255 shown; the rationales for these additions are described in the next section.

256 Table 1. Properties of the actual model and the initial operational model.

Model Feature	Actual Model	Initial Operational Model	When Features Added
Formation Geometry	From geologic model: dipping storage formation about 500 m thick; lateral extent: 47 km by 60 km; undulating caprock/formation interface	Same as Actual Model	Year 0 (initial)
Lateral Boundary Conditions	Three closed lateral boundaries represent sealing faults, open updip lateral boundary represents transition to a shallower aquifer system	Same as Actual Model	Year 0 (initial)
Layering	20 layers from well log, range of ϕ : 0.24 – 0.35, range of k_h : 3.7 – 551 mD, range of k_v : 0.008 – 188 mD	No layers: uniform $\phi = 0.3$, $k_h = 24$ mD, $k_v = 1.2$ mD	Year 1
Faults	Two vertical faults, $k_h = 5$ mD, $k_v = 200$ mD	No faults	1st fault -Year 2, 2nd fault -Year 10
Lateral Heterogeneity	Stochastic heterogeneity (GSLIB, Deutsch and Journel 1992); permeability roughly log-normal, conditioned to well log, range of ϕ : 0.025 – 0.56, range of k_h : 0.015 mD – 68 D, log-mean $k_h = 22$ mD; range of k_v : 0.014 nD – 63 mD	None	
Multi-phase flow properties	Hysteretic van Genuchten (Doughty, 2007); S_{lr} , m , S_{grmax} depend on permeability: range of $S_{lr} = 0.03 – 0.42$, range of m : 0.86 – 1.25, range of $S_{grmax} = 0.027 – 0.50$; Leverett scaling for P_{c0}	Non-hysteretic van Genuchten (1980): $S_{lr} = 0.116$, $m = 1.052$, $S_{gr} = 0$ during injection period; $S_{gr} = 0.2$ during post-injection period	Year 25, Year 50
Initial Conditions	Hydrostatic pressure distribution, geothermal temperature gradient, gas-phase CH ₄ in localized attics up against lower-most caprock	Same but no CH ₄	Year 5

258 **4. Results**

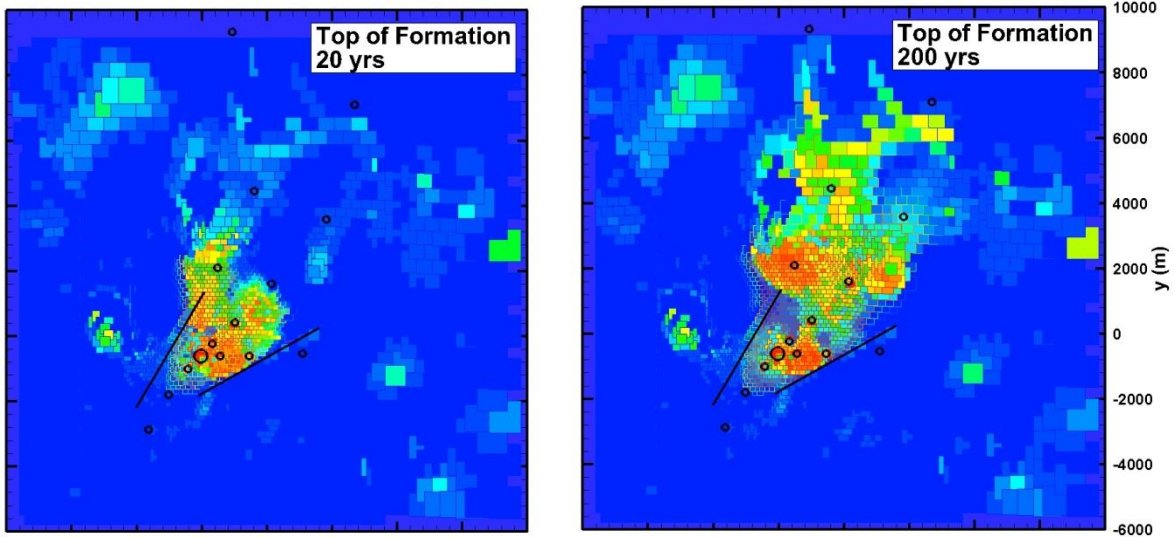
259 **Actual Model**

260 *Complete information*

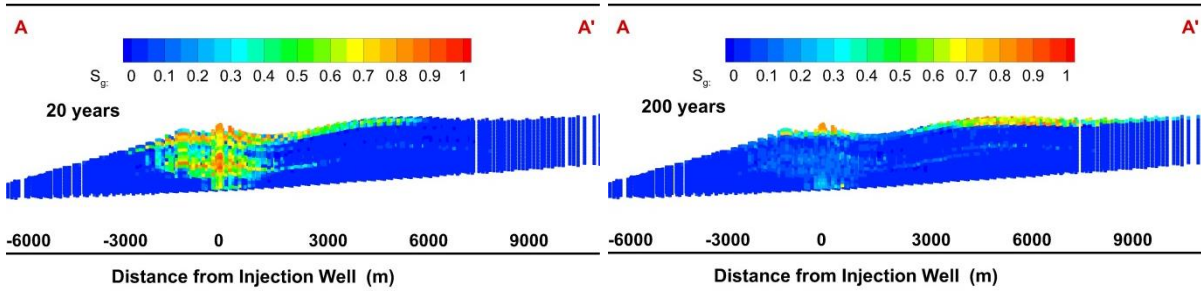
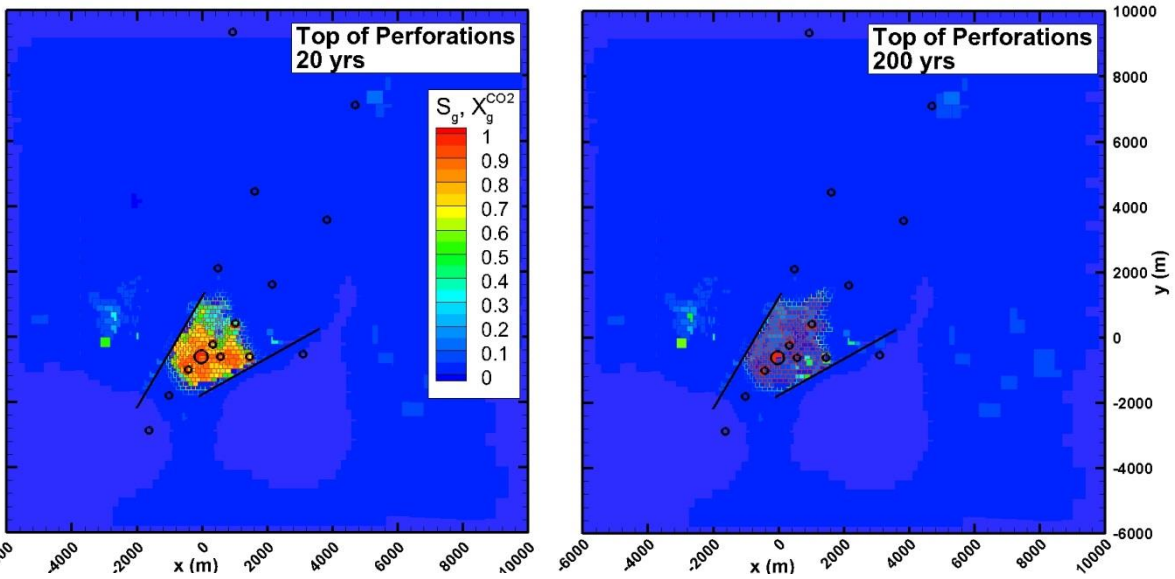
261 Figure 8 shows layer and cross-section views of the CO₂ plume at the end of the injection period,
262 20 years, and at the end of the extended simulation at 200 years. Note that CO₂ moves readily
263 upward in the formation from the perforated interval to the top of the formation. As the CO₂
264 plume develops, it is surrounded by a halo of free-phase CH₄, which forms when CH₄ dissolved
265 in the brine exsolves into the gaseous phase provided by the injected CO₂ (e.g., Oldenburg et al.,
266 2013).

267 Figure 9 shows the maximum pressure change in the uppermost layer of the storage formation
268 which occurs at the end of the injection period. The black contour line indicates a pressure
269 change of 0.1 MPa, which would be sufficient to lift fluid 10 m.

270



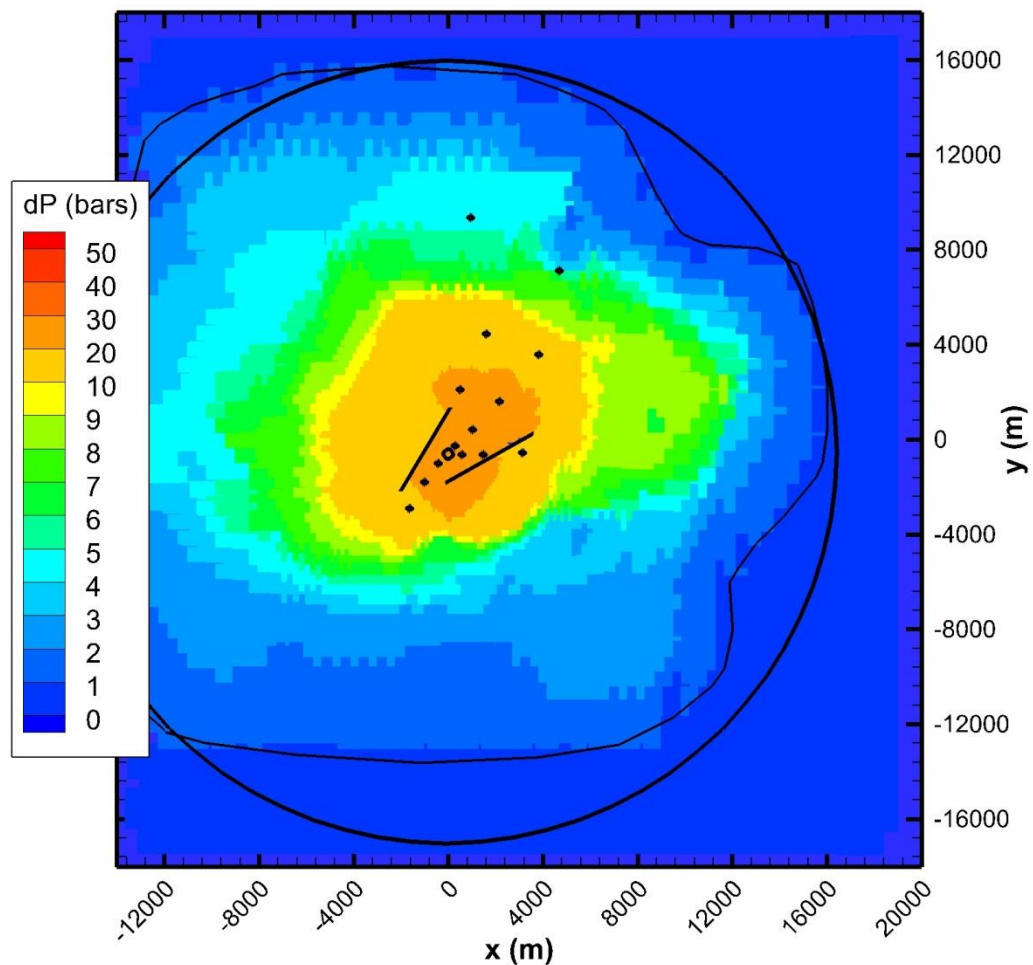
271



272

273 *Figure 8. Distribution of CO₂ at the end of the injection period (eft column) and at the end of the*
 274 *simulation (right column). In the top four frames, the cell fill color indicates gas saturation and*
 275 *the cell outline color indicates CO₂ mass fraction. The location of the cross-sections is shown in*
 276 *Figure 3.*

277



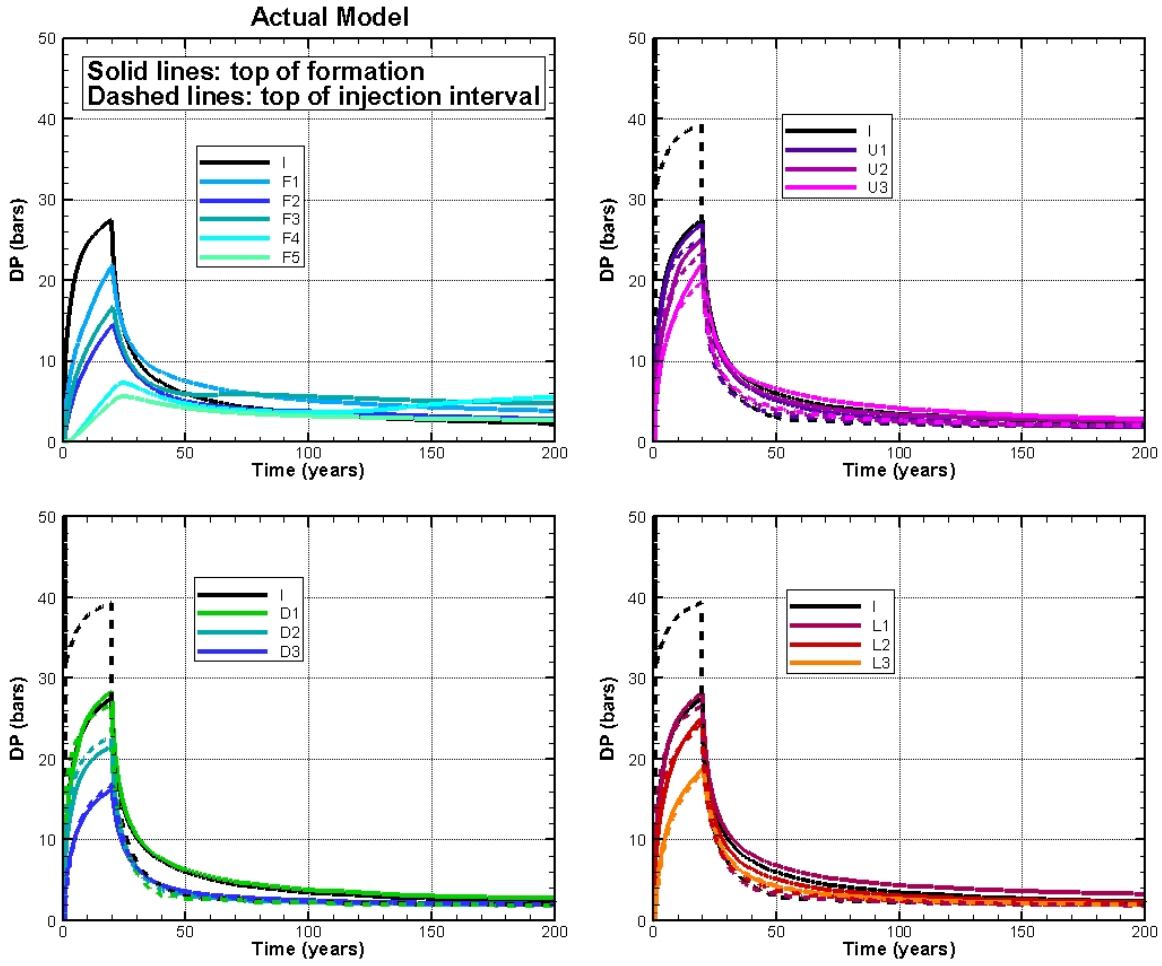
278

279 *Figure 9. The layer at the top of the storage formation, showing the pressure increase at the end*
 280 *of the injection period. The thin black line outlines the region with $dP > 1$ bar and the thick*
 281 *black line approximates this region with a circle of radius 16.5 km.*

282 ***Monitoring Data***

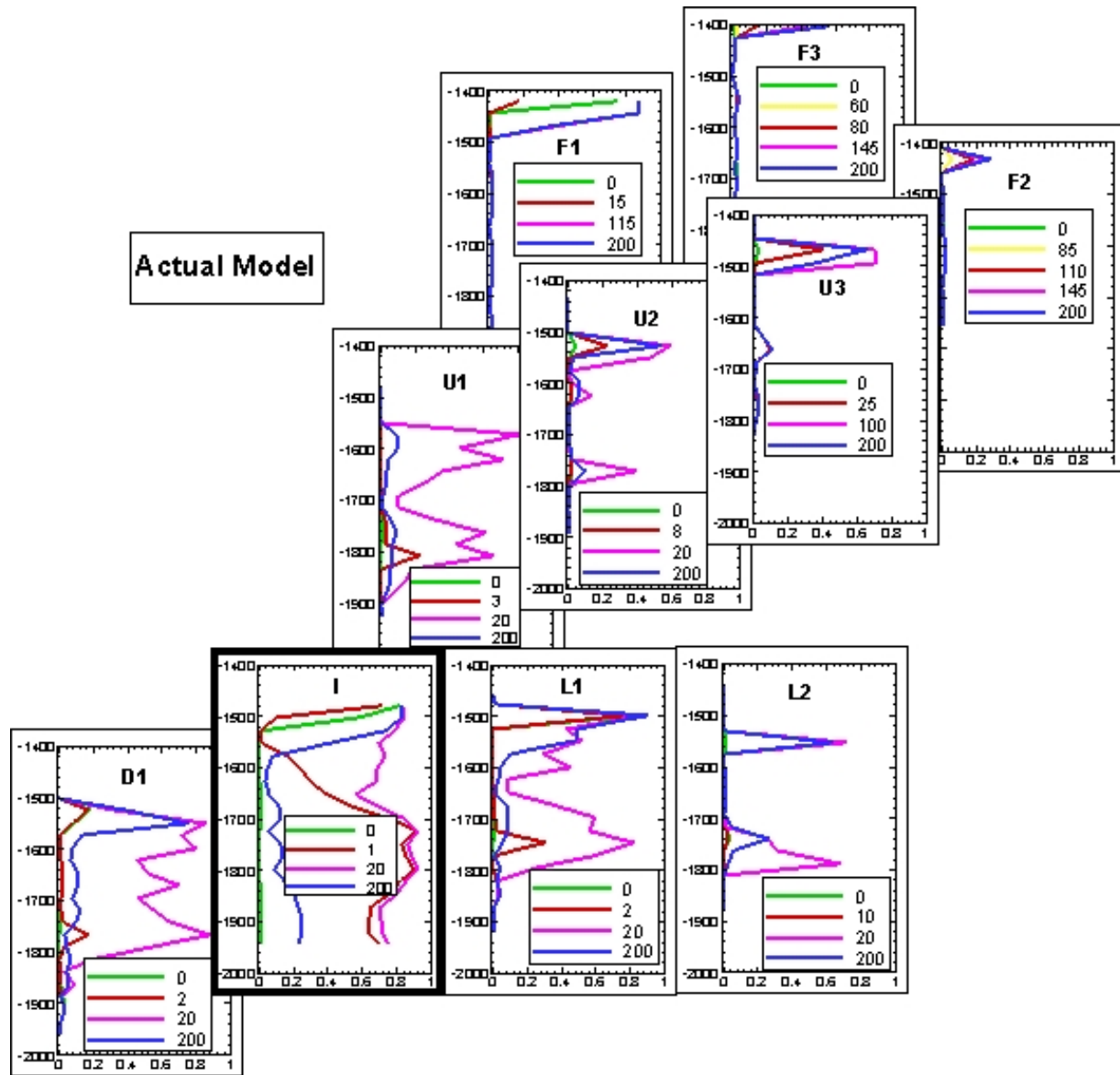
283 Figures 8 and 9 provide a complete view of the evolution of the CO₂ plume and pressure pulse,
 284 but we will not use these data in operational model development. Rather, to demonstrate the
 285 evolution of conformance uncertainty over time, we limit ourselves to monitoring data that
 286 would be obtained from monitoring wells consisting of pressure transients (Figure 10) and
 287 saturation profiles (Figures 11 and 12). Moreover, we do not use the entire 200-year duration of

288 these data, but just the portion up to the year in which the model development is occurring. All
289 wells show pressure changes very soon after injection starts (Figure 10), but saturation changes
290 occur later at more distant monitoring wells (Figure 11). The sequence of saturation changes at
291 the injection well (Figure 12) is typical of the nearby monitoring wells, in that the first response
292 is at the depth of the perforated interval, with upward movement of the CO₂ plume occurring
293 later during the injection period and continuing through the full simulation period. In contrast, in
294 more distant monitoring wells, the CO₂ plume arrives in the uppermost portion of the storage
295 formation and stays there at all subsequent times.



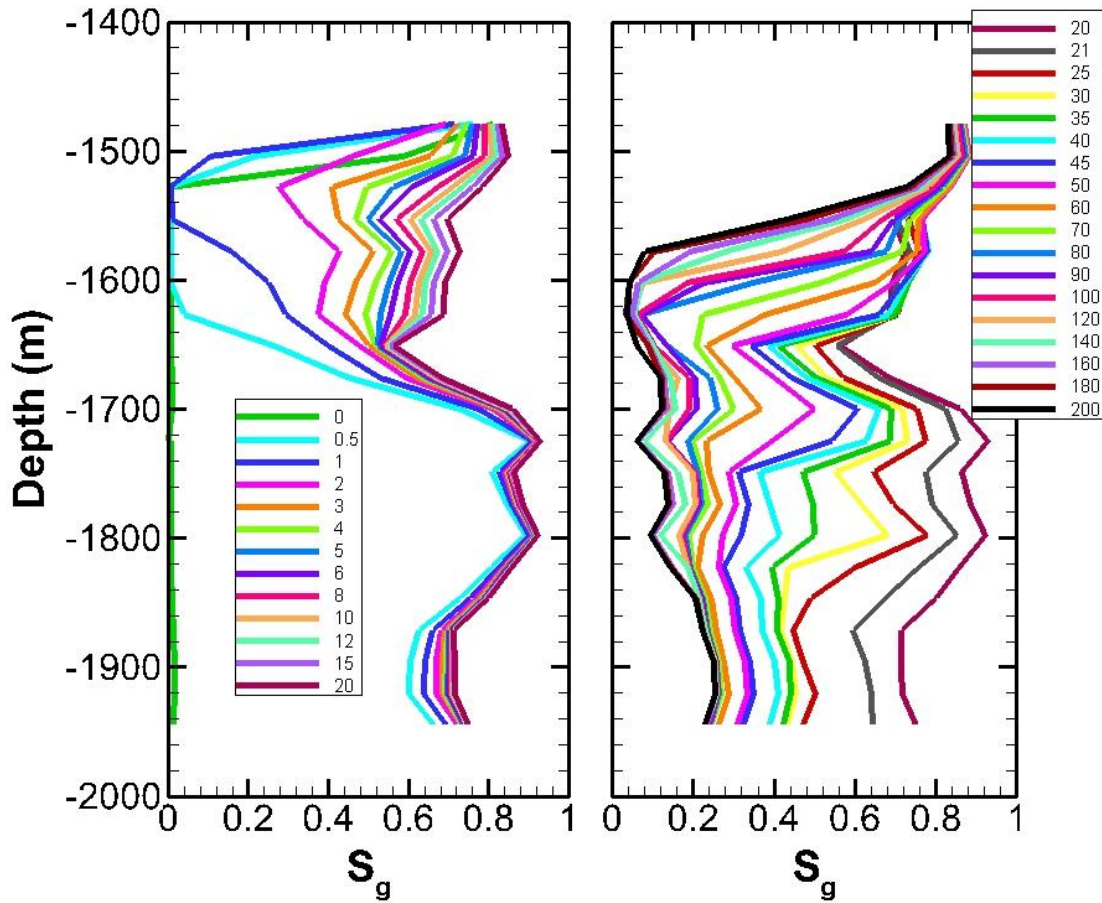
296

297 *Figure 10. Actual model pressure transients. Legends show well names; see Figure 6 for*
 298 *locations. The upper left frame shows the far wells, and the other three frames show the U, D,*
 299 *and L wells. The injection-well response is shown in each frame for reference. Dashed and solid*
 300 *lines show the response at the top of the perforated interval and the top of the storage formation,*
 301 *respectively.*



302

303 *Figure 11. Selected saturation profiles in the monitoring wells for the actual model: green is the*
 304 *initial condition (gas is CH₄), yellow shows first increase in CH₄, red shows first increase in*
 305 *CO₂, pink is the maximum S_g, and blue is the final condition at 200 years. Of the 15 wells*
 306 *available for monitoring, saturation changes are only observed in these 10 wells. X axis is gas*
 307 *saturation S_g; Y axis is depth in meters; legend is profile time in years. The layout of profile*
 308 *plots corresponds to well location (Figure 6).*



309

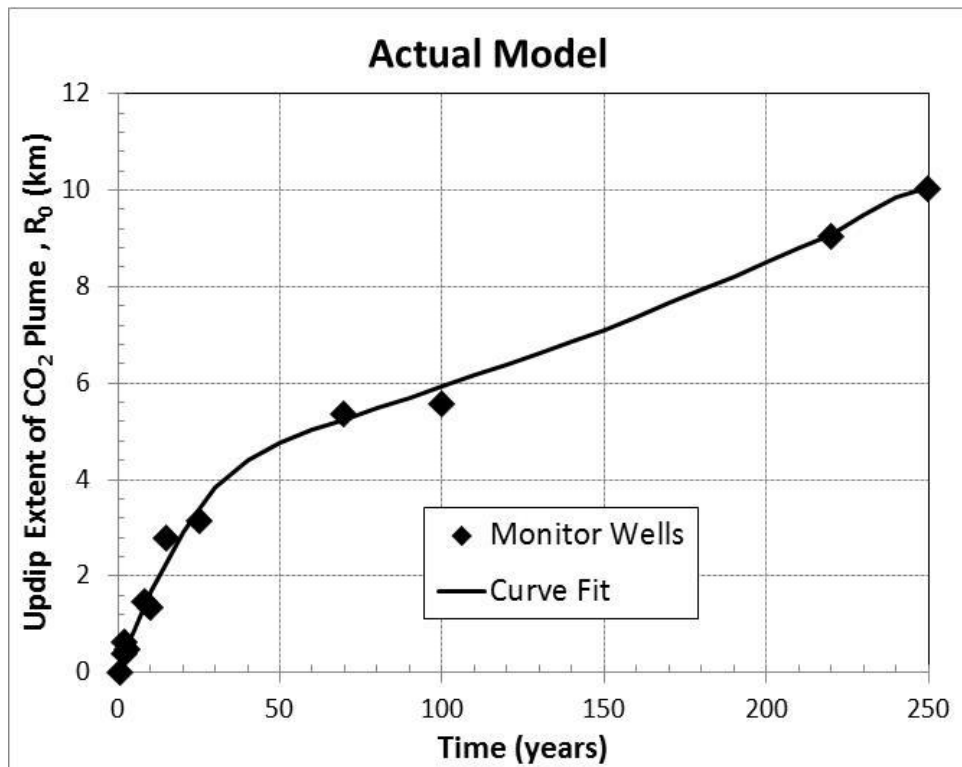
310 *Figure 12. All saturation profiles in the injection well for the actual model. The legend numbers*
 311 *indicate profile time in years. The left-hand-side frame shows times during the injection period*
 312 *and the right-hand-side frame shows times during and beyond the 50-year PISC period. Colors*
 313 *are arbitrarily chosen to enhance profile visibility.*

314

315 ***Metrics for comparing models***

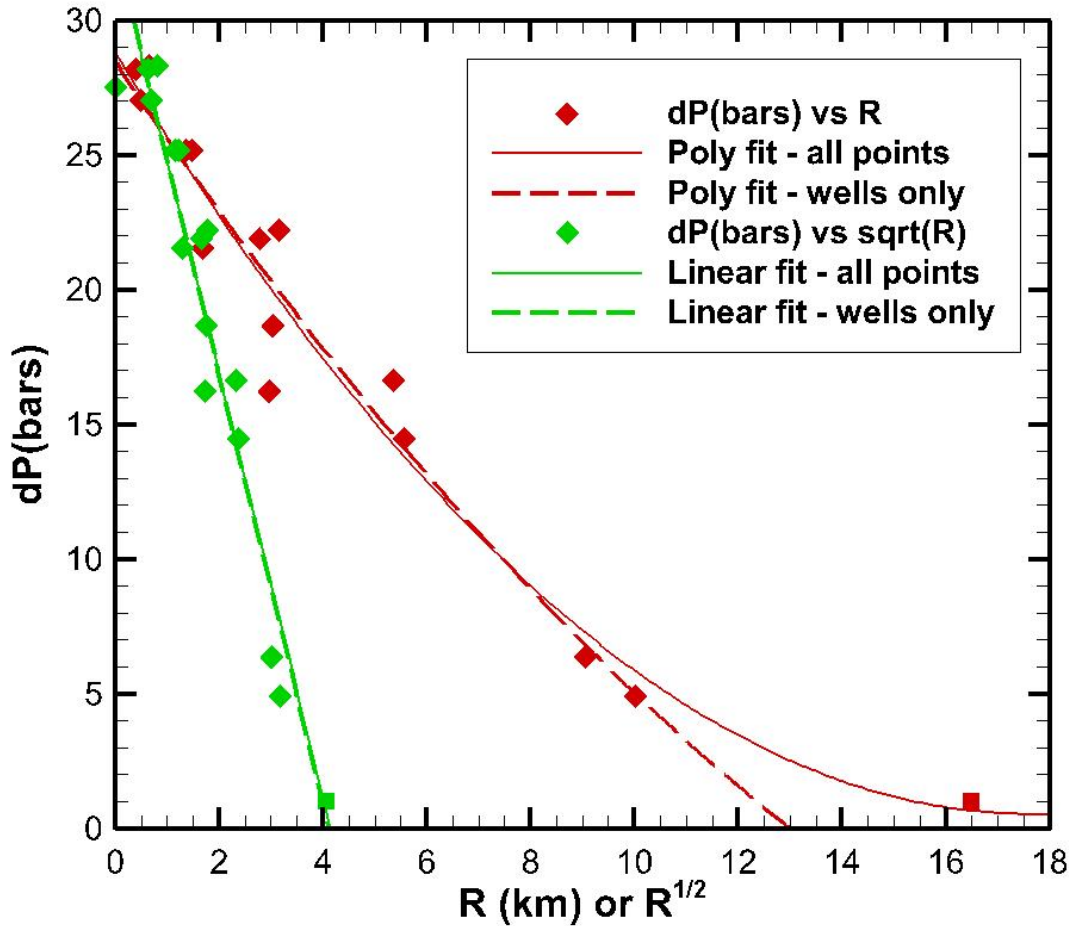
316 The two key metrics we use to judge concordance between the actual system and the operational
 317 models are (1) the extent of the CO₂ plume updip migration at the end of the 200-year simulation
 318 period, denoted R_0 , and (2) the extent of the pressure pulse at the end of the injection period,
 319 denoted R_1 , as inferred from monitoring well data. Figure 13 shows R_0 as a function of time for
 320 the actual model. Each symbol shows the time at which the CO₂ plume arrives at a monitoring
 321 well, quantified as a minimum gas saturation of 0.02 and a minimum CO₂ mass fraction of 0.02.

322 Figure 14 shows the maximum pressure change at the monitoring wells at the end of the injection
 323 period, and R_I , taken from Figure 9. The pressure profiles are plotted against distance R from the
 324 injection well, and also against $R^{1/2}$. The goal is to use just the points taken from the monitoring
 325 wells, and extrapolate to estimate R_I . Plotting dP versus R does not enable a good extrapolation;
 326 a polynomial fit yields a very inaccurate estimate of R_I . Plotting dP versus $R^{1/2}$ does much better,
 327 allowing a linear fit that yields a reasonable estimate of R_I . This provides a recipe for
 328 determining the extent of the pressure pulse for the operating models using only monitoring well
 329 data.



330
 331 *Figure 13. Updip extent of the CO₂ plume, R₀, for the actual model.*

Pressure Change at Top of Storage Formation at End of Injection Period



332
 333 *Figure 14. Red diamonds: maximum pressure change at monitoring wells at the end of the*
 334 *injection period, plotted against distance from the injection well, R. Green diamonds: maximum*
 335 *pressure change at monitoring wells plotted against R^{1/2}. Squares show P(R₁)= 1 bar. The solid*
 336 *lines show best-fit polynomial (red) and linear (green) functions including monitoring well data*
 337 *and P(R₁). The dashed lines show fits including monitoring well data only.*

338 **Operational Model Development**

339 Table 2 shows a summary of operational model development. Further details are provided below.

340 *Year 1*

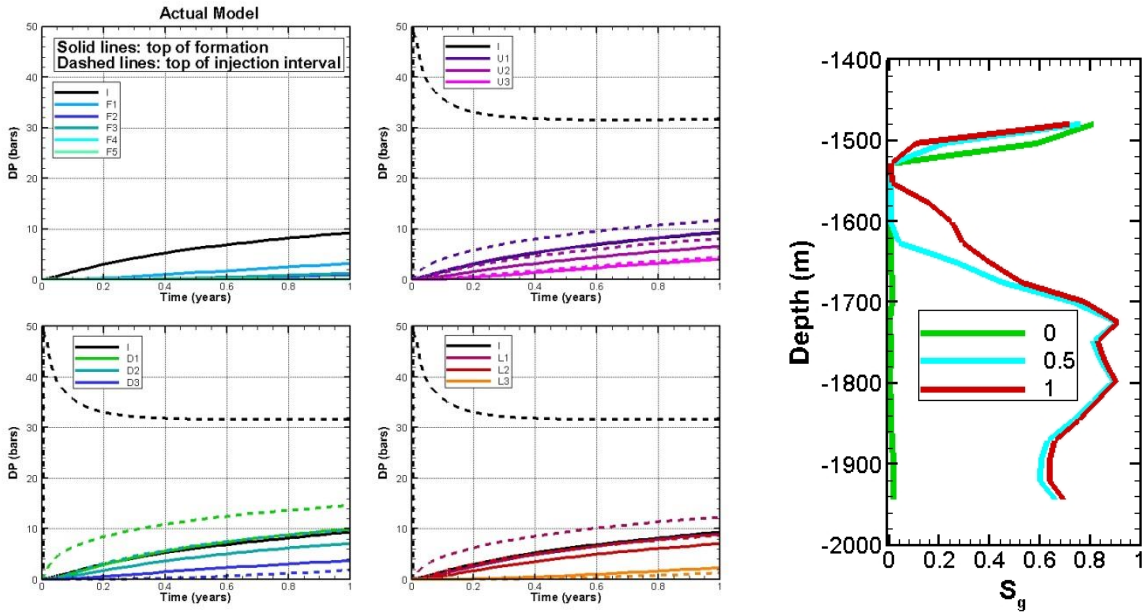
341 The actual model monitoring data for the first year are shown in Figure 15. Note that at one year

342 all but the most distant monitoring wells show a pressure response, but only the injection well

343 shows any change in saturation. At the perforated interval, saturation increase indicates the

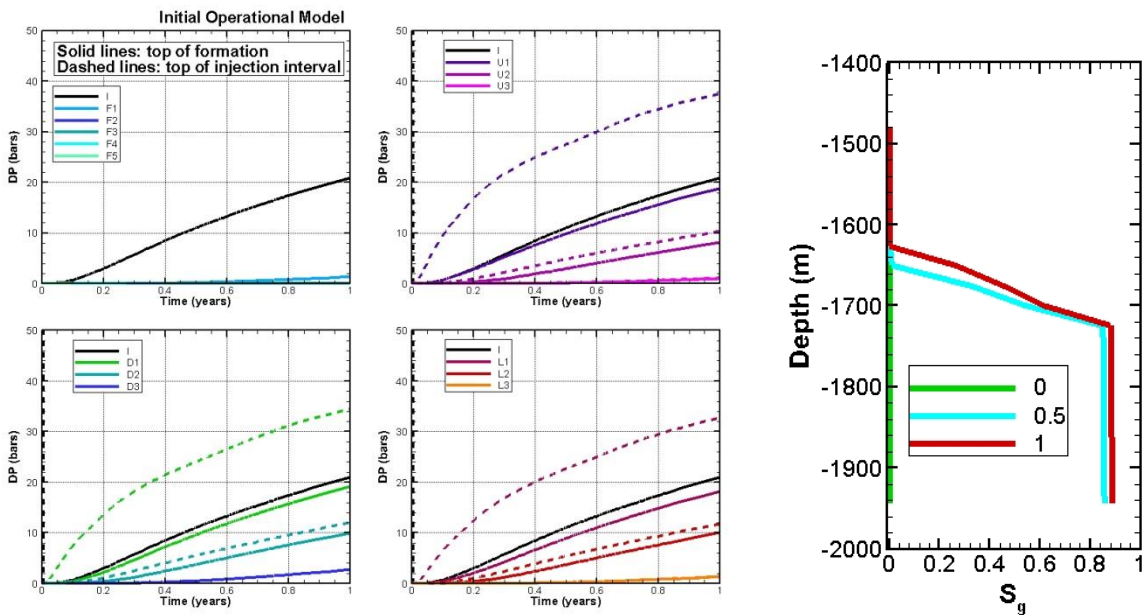
344 growing presence of the injected CO₂. Near the top of the formation, the small saturation
345 decrease indicates less CH₄.

346 The corresponding forecast results for the initial operational model are shown in Figure 16. For
347 the operational model, which is homogeneous, the pressure increases for the injection well and
348 nearby monitoring wells are far too large, whereas the pressure changes for more distant
349 monitoring wells tend to be too small. Also, the difference between pressure change at the
350 perforated interval and at the top of the storage formation tends to be too large. Together, these
351 observations suggest that operational-model permeability should be increased. The operational-
352 model saturation profile at the depth of the perforated interval is too uniform, and in particular
353 saturation is too large in the deeper portion of the perforated interval, suggesting that variable-
354 permeability layers should be used. The gradual increase in operational-model saturation above
355 the perforated interval provides information on the vertical permeability there, which seems
356 about right. Because CH₄ is not included in the operational model, the shallow S_g peak observed
357 in the actual model is absent.



358

359 *Figure 15. Actual model Year 1 results. (a) pressure transients, (b) saturation profiles at Well I.*

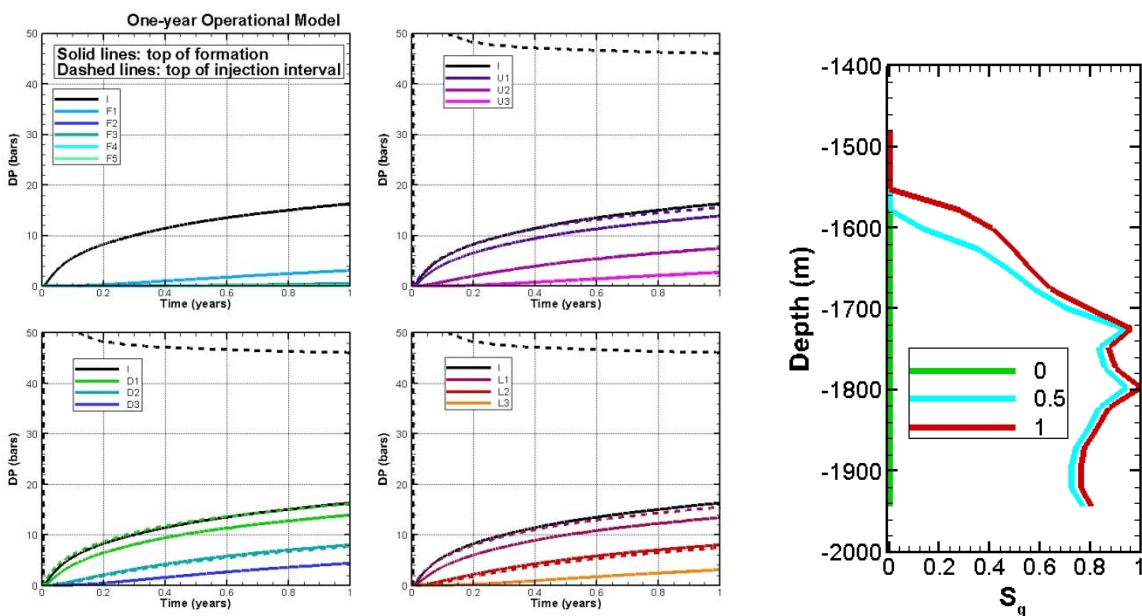


360

361 *Figure 16. Initial operational model Year 1 forecast: (a) pressure transients, (b) saturation*
 362 *profiles at Well I. The pressure change at the perforated interval in the injection well is off scale*
 363 *at about 100 bars.*

364 After several manual iterative updates of the operational model, including increasing overall
 365 permeability and introducing a layered structure at the depth of the perforated interval, the final
 366 one-year operational model hindcast results are shown in Figure 17. Horizontal permeability,

367 which was uniform at 24 mD in the initial operational model, now varies from 3 to 121 mD over
 368 the perforated interval and is uniform at 121 mD above the perforated interval. Comparing
 369 Figures 15, 16, and 17 indicates that observations after one year allow updates to the operational
 370 model properties that greatly improve the pressure and saturation concordance to the actual
 371 model compared to the initial operational model, although most operational-model pressure
 372 responses are still a few bars too big.

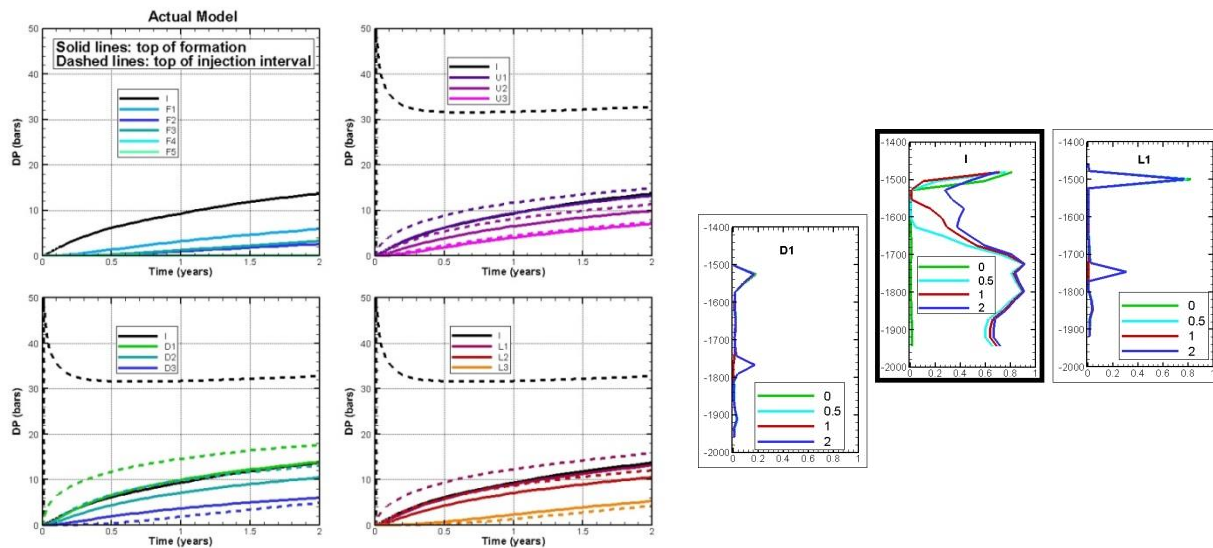


373
 374 *Figure 17. Updated operational model Year 1 hindcast: (a) pressure transients, (b) saturation*
 375 *profiles at Well I.*

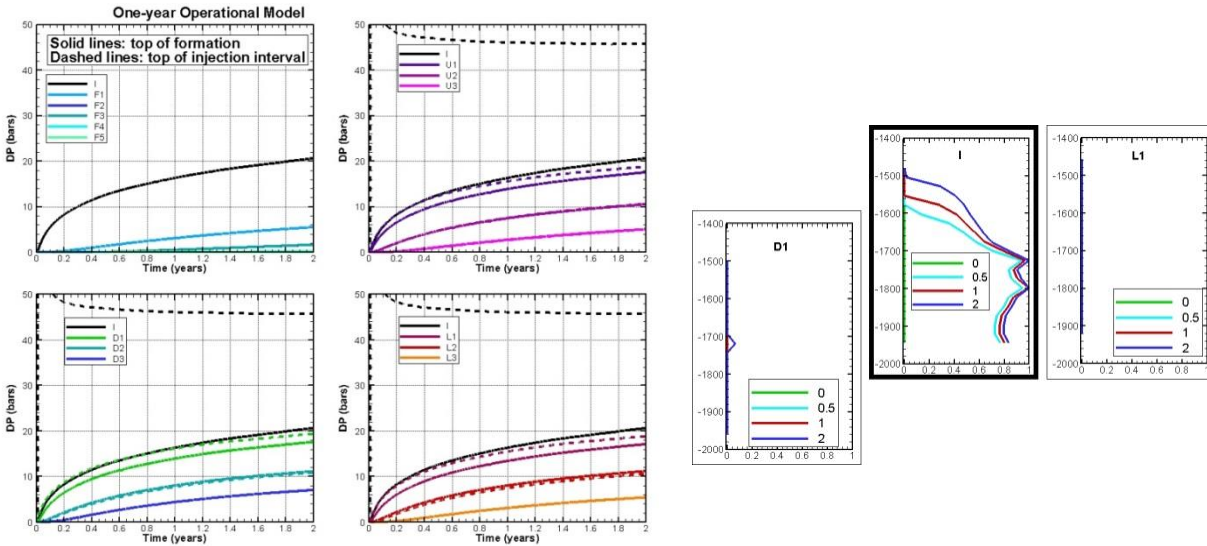
376 **Year 2**

377 The actual model monitoring data for the second year are shown in Figure 18. At two years the
 378 injection well and two nearby monitoring wells show saturation changes relative to initial
 379 conditions. The shallowest gas-saturation peak in each well represents attic gas (CH₄). The
 380 corresponding forecasts using the updated one-year operational model are shown in Figure 19.
 381 For the one-year operational model forecast for two years, the magnitude of the pressure change
 382 in the injection well at the perforated interval is significantly too large (~47 bars compared to

383 ~32 bars), but all the other pressure changes are within about 5 bars of the actual model. Note
 384 that the actual model shows a bigger separation between pressure response for Well L2 and Well
 385 L3 than does the operational model, suggesting that there should be a low-permeability zone
 386 separating the two wells. The operational-model saturation response at the perforated interval
 387 depth in Wells D1 and L1 is too small, suggesting that the variability of layer permeability
 388 should be larger. A small CO₂ peak in the actual-model injection-well saturation profile above
 389 the perforated interval suggests that a layered structure is needed for the shallow portion of the
 390 storage formation.



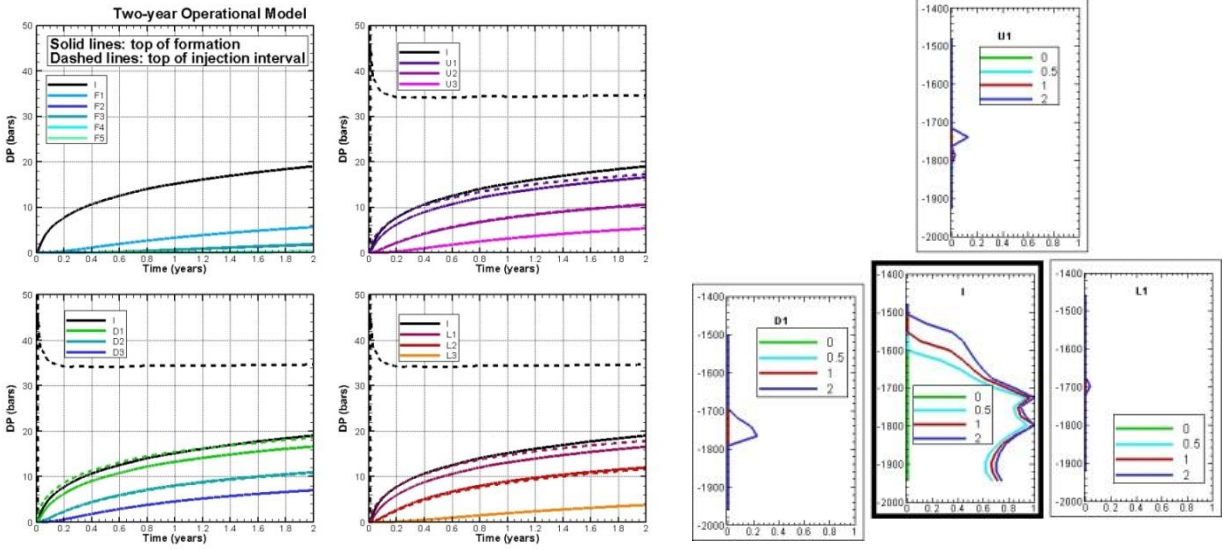
391
 392 *Figure 18. Actual model Year 2 results: (a) pressure transients, (b) saturation profiles.*



393

394 *Figure 19. One-year operational model Year 2 forecast: (a) pressure transients, (b) saturation*
 395 *profiles.*

396 After several model updates directed at improving the Year 2 concordance between actual and
 397 operational models, we set up a layered structure above the depth of the perforated interval,
 398 modified permeabilities at the perforated interval to encourage preferential flow, and introduced
 399 a fault between Wells L2 and L3. The final two-year operational model hindcast results are
 400 shown in Figure 20. Comparison of Figures 18, 19, and 20 indicates that the two-year
 401 operational model generally improves the concordance to the actual model compared to the one-
 402 year operational model. In particular, the final pressure change in the injection well at the
 403 perforated interval for the operational model is much closer to the actual value (~35 bars
 404 compared to ~32 bars), and the difference in pressure response between Wells L2 and L3 is
 405 larger, consistent with a low-permeability fault between them. The operational-model S_g peak
 406 arrival is still a little late in Wells D1 and L1, and a little early in Well U1, and the CO₂ peak
 407 developing above the perforated interval in Well I is not well represented. The shallow CH₄
 408 peaks observed in Wells D1, I, and L1 in the actual model are absent in the operational model.



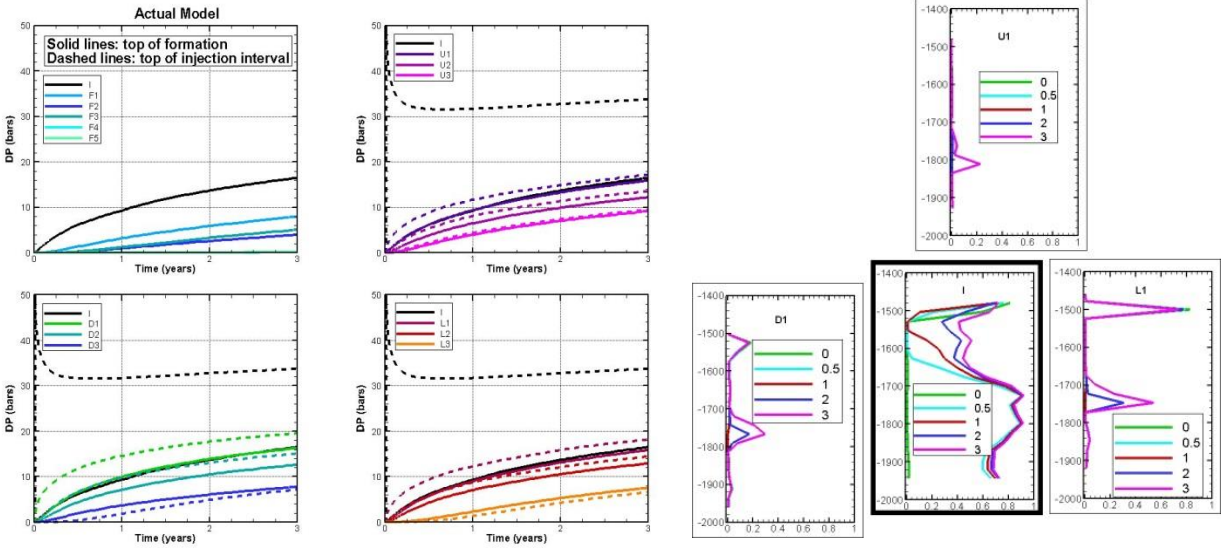
409

410 *Figure 20. Two-year operational model Year 2 hindcast: (a) pressure transients, (b) saturation*
 411 *profiles.*

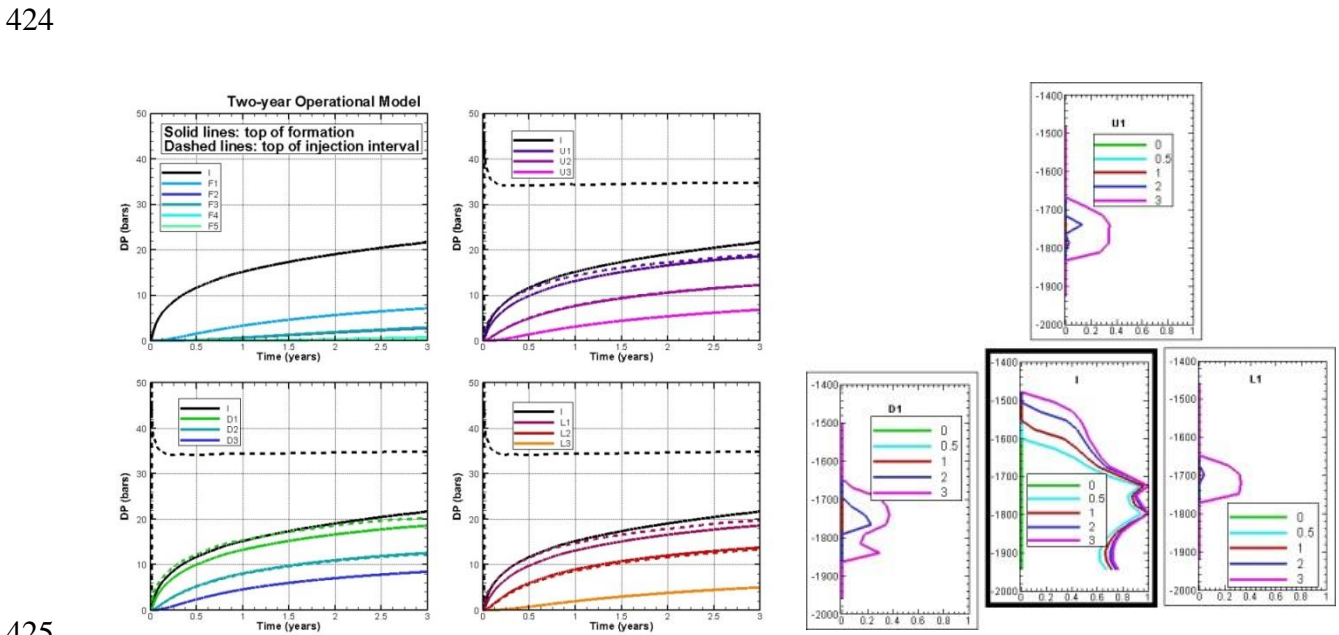
412

413 **Year 3**

414 Continuing with the process of comparison of actual to operational models, the actual model
 415 monitoring data for the third year are shown in Figure 21. At three years the injection well and
 416 three nearby monitoring wells show saturation changes relative to initial conditions. The
 417 corresponding forecast results for the two-year operational model are shown in Figure 22. For
 418 the operational model, at the injection well and nearby monitoring wells, pressure change is
 419 generally a few bars too big. S_g profiles representing CO₂ peaks are generally consistent between
 420 the actual and operational models, but the actual peaks are sharper. The shallow CH₄ peaks
 421 observed in Wells D1, I, and L1 in the actual model are absent in the operational model.



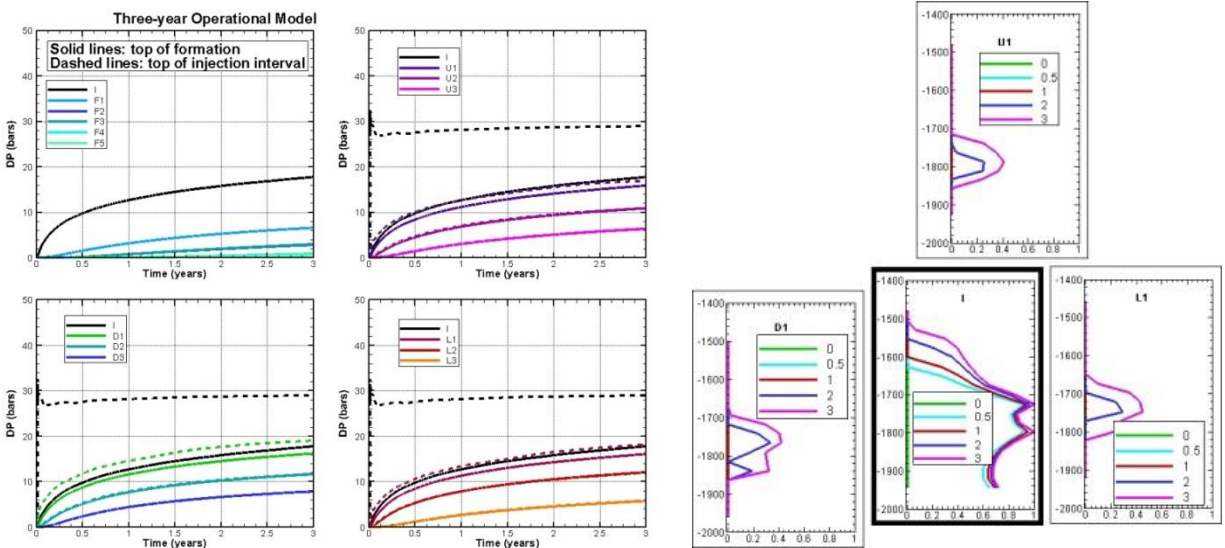
422
 423 *Figure 21. Actual model Year 3 results: (a) pressure transients, (b) saturation profiles.*



425
 426 *Figure 22. Two-year operational model Year 3 forecast: (a) pressure transients, (b) saturation*
 427 *profiles.*

428
 429 After several operational model updates including doubling the permeability at the depth of the
 430 perforated interval, decreasing the permeability of some layers above the depth of the perforated
 431 interval, and increasing fault permeability from 5 mD to 15 mD, the final three-year operational

432 model hindcast results are shown in Figure 23. Comparing Figures 21, 22, and 23 indicates that
 433 the three-year operational model somewhat improves the concordance to the actual model
 434 compared to the two-year operational model. Compared to the two-year operational model,
 435 pressure changes are a little smaller in the injection well (which is now about 5 bars too small at
 436 the perforated interval) and nearby monitoring wells (which are now in better agreement with the
 437 actual model). Operational-model S_g peaks at nearby monitoring wells are a little bigger, which
 438 is generally in better agreement with the actual model. The shallow CH_4 peaks observed in Wells
 439 D1, I, and L1 in the actual model are absent in the operational model.

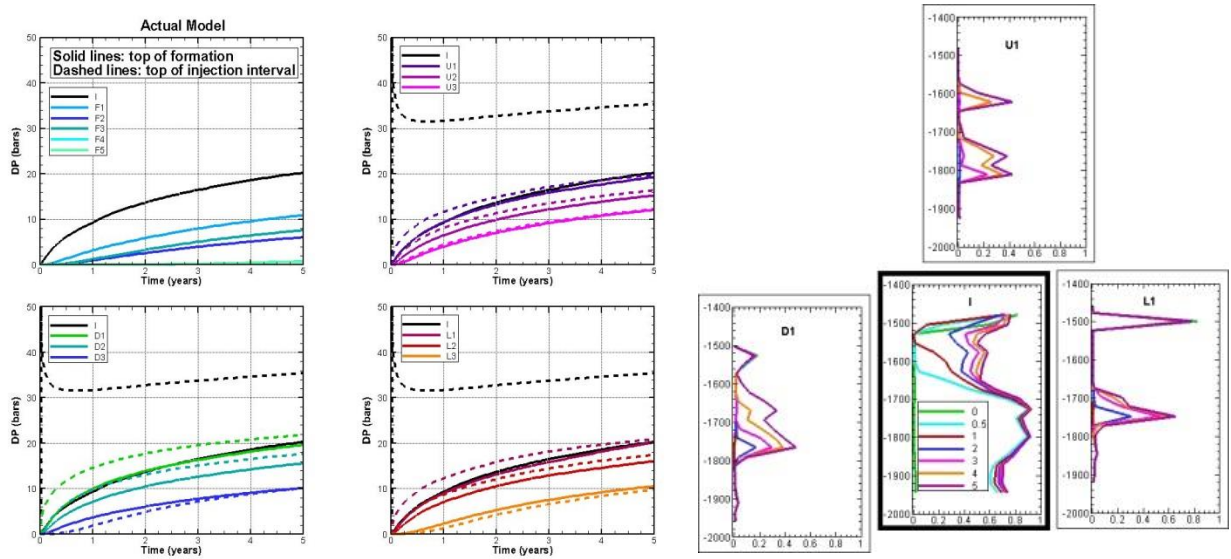


440
 441 *Figure 23. Three-year operational model Year 3 hindcast: (a) pressure transients, (b) saturation*
 442 *profiles.*

443
 444 **Year 5**

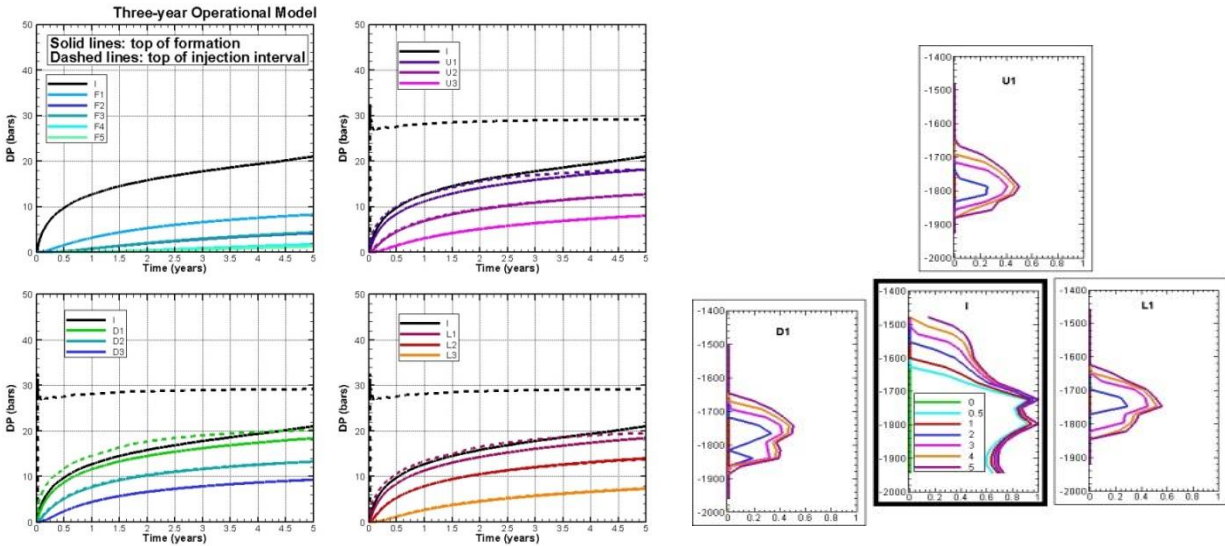
445 The actual model monitoring data for the fifth year are shown in Figure 24—we skip Year 4
 446 consistent with the idea that the frequency of model updating should decrease as understanding
 447 of the system increases. At five years the injection well and three nearby monitoring wells show
 448 saturation changes relative to initial conditions. The corresponding forecast results for the three-

449 year operational model are shown in Figure 25. With a longer time period available for
 450 comparing pressure transients, by five years it is apparent that the operational model transients
 451 show too much curvature, i.e., they increase too rapidly at first, then level off too much later.
 452 After unsuccessful attempts to decrease curvature by increasing storativity by increasing rock
 453 compressibility, it was decided that the presence of the additional gas phase in the form of a
 454 natural gas cap (CH₄) could provide the additional storativity needed. Thus CH₄ gas was added
 455 to the operational model in a pre-injection phase of model development in the same manner as
 456 the initial condition of the actual model was developed, i.e., by introducing it uniformly at a low
 457 saturation and allowing it to migrate upward into formation attic spaces during an initial gravity
 458 equilibration.



459
 460 *Figure 24. Actual model Year 5 results: (a) pressure transients, (b) saturation profiles.*

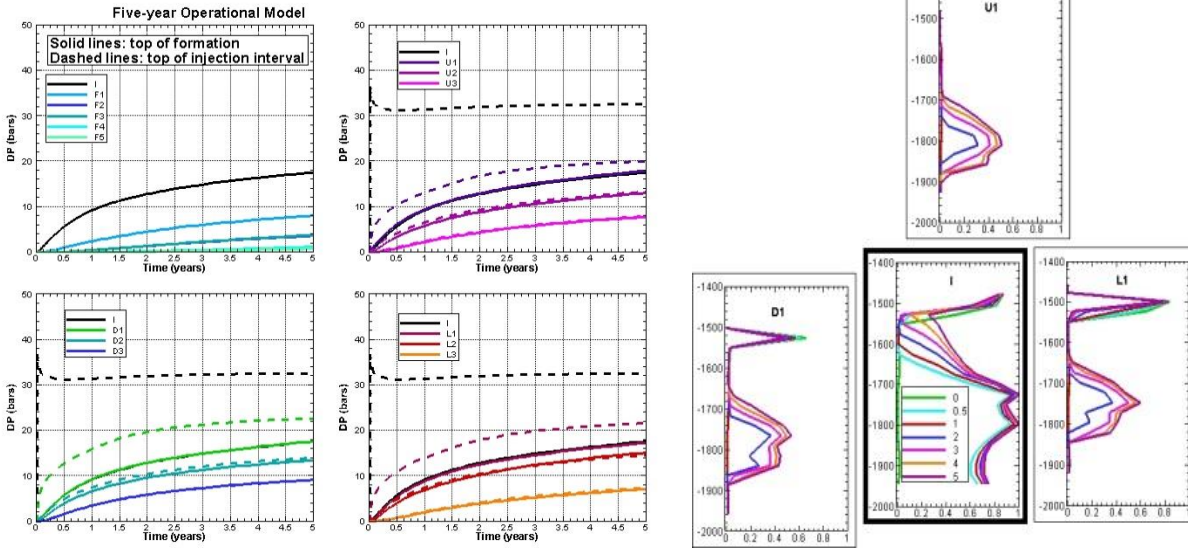
461



462

463 *Figure 25. Three-year operational model Year 5 forecast: (a) pressure transients, (b) saturation*
 464 *profiles.*

465 After several model update iterations, the final five-year operational model hindcast results are
 466 shown in Figure 26. The differences from the three-year operational model are the inclusion of
 467 CH₄ in the attic space and a decrease in the permeabilities just above the perforated interval.
 468 Comparing Figures 24, 25, and 26 indicates that the five-year operational model somewhat
 469 improves the concordance to the actual model compared to the three-year operational model.
 470 Compared to the three-year operational model, pressure changes are a little smaller in the
 471 injection well (which is now about 5 bars too small at the perforated interval) and nearby
 472 monitoring wells (which are now in better agreement with the actual model). Overall curvature
 473 of the dP versus time curve is only slightly better than before. Operational-model S_g peaks at
 474 nearby monitoring wells at the depth of the perforated interval, representing injected CO₂, are a
 475 little bigger, which is generally in better agreement with the actual model, and shallow S_g peaks
 476 showing CH₄ are now included.



477

478 *Figure 26. Five-year operational model Year 5 hindcast: (a) pressure transients, (b) saturation*
 479 *profiles.*

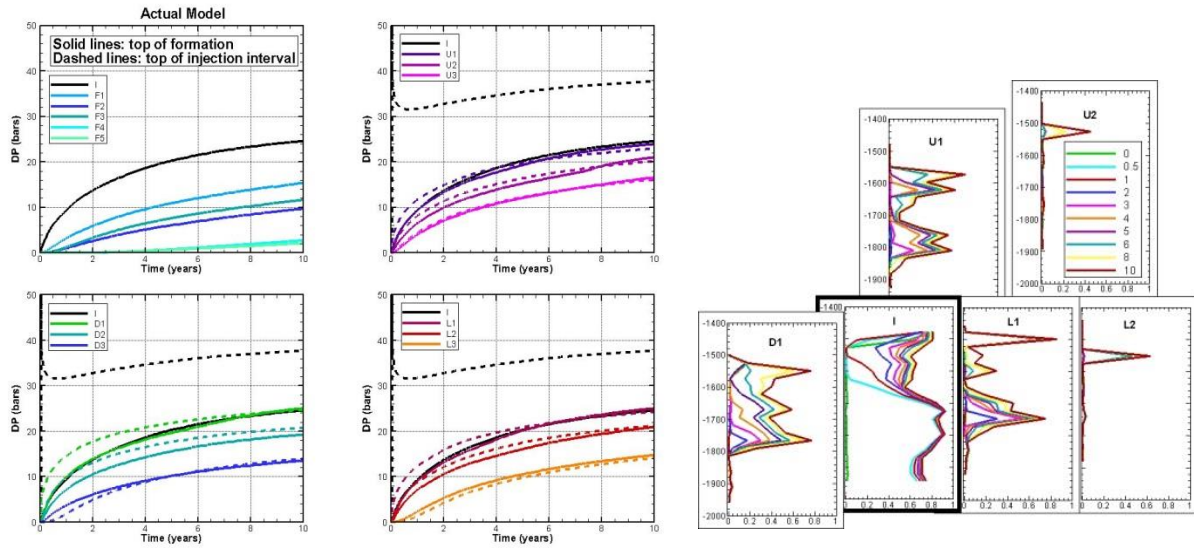
480

481 ***Year 10***

482 The actual model monitoring data for the tenth year are shown in Figure 27. At ten years the
 483 injection well and five nearby monitoring wells show saturation changes relative to initial
 484 conditions. The corresponding forecast results for the five-year operational model are shown in
 485 Figure 28. For the operational model, the curvature of the dP versus time curve is still too large
 486 and most dP values are too small. One possible way to decrease the curvature would be to make
 487 the overall flow geometry more linear and less radial, which could be accomplished by placing a
 488 low-permeability zone west of the well field. Such a zone should also increase the magnitude of
 489 dP at all near-injection monitoring wells. Also, the separation between the Well L2 and Well L3
 490 pressure response curves is too big, suggesting that the L2-L3 fault permeability should be
 491 increased. The actual model saturation profiles show several peaks above the perforated interval,
 492 representing injected CO_2 that is moving upward through the formation. The operational-model

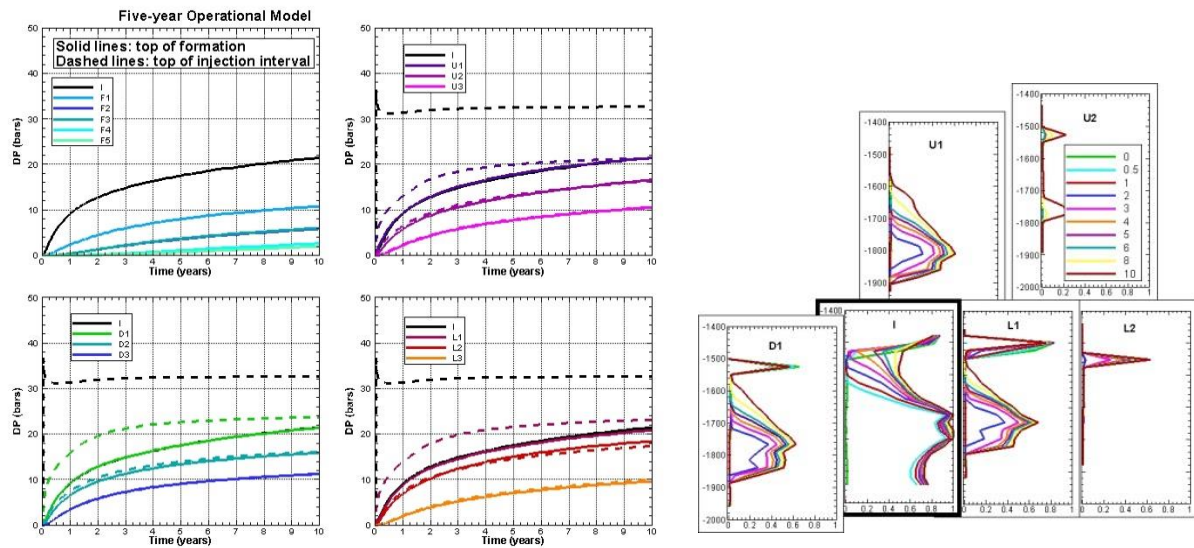
493 saturation profiles do not show these peaks, suggesting the need for higher permeabilities in the
 494 layers above the perforated interval.

495



496

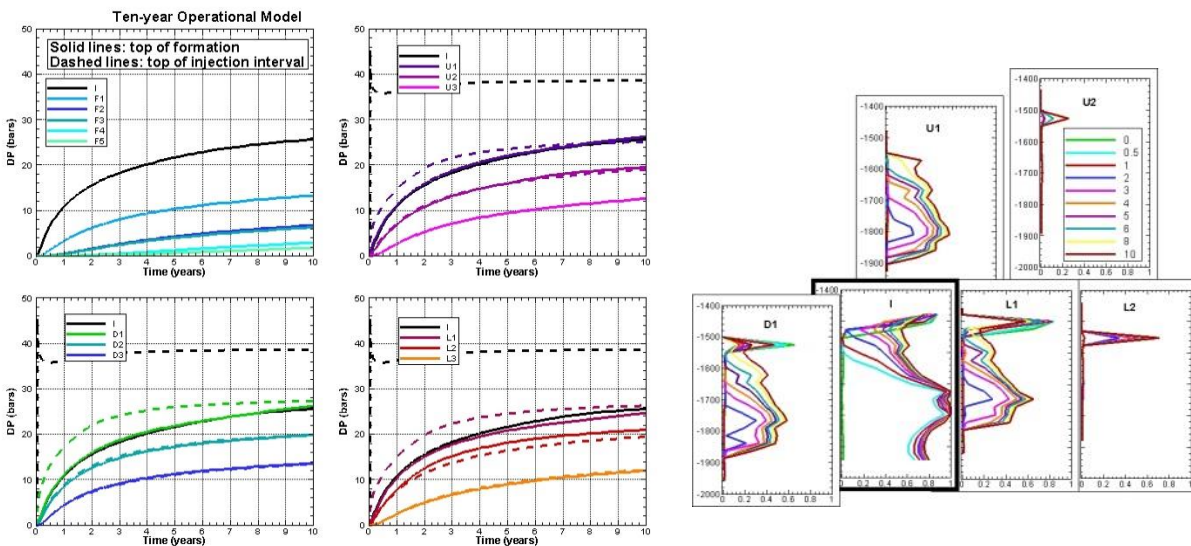
497 *Figure 27. Actual model Year 10 results: (a) pressure transients, (b) saturation profiles.*



498

499 *Figure 28. Five-year operational model Year 10 forecast: (a) pressure transients, (b) saturation*
 500 *profiles.*

501 After several operational model update iterations, the final ten-year operational model was
 502 updated to include a new fault to the west of the well field with a low permeability of 1 mD, a
 503 small increase in the permeabilities just above the perforated interval with a corresponding small
 504 decrease in the permeabilities at the perforated interval, and an increase in the L2-L3 fault
 505 permeability from 15 to 30 mD. The final ten-year operational model hindcast results are shown
 506 in Figure 29. Comparing Figures 27, 28, and 29 indicates that the ten-year operational model
 507 somewhat improves the concordance to the actual model compared to the five-year operational
 508 model. Compared to the five-year operational model, pressure changes are a little bigger in the
 509 injection well and nearby monitoring wells (which are now in better agreement with the actual
 510 model). The separation between Well L2 and Well L3 pressure curves is slightly smaller. The
 511 overall curvature of the dP versus time curve is only slightly better than before. Operational-
 512 model S_g peaks at nearby monitoring wells at depths above the perforated interval, representing
 513 injected CO_2 , are a little bigger, which is generally in better agreement with the actual model.
 514

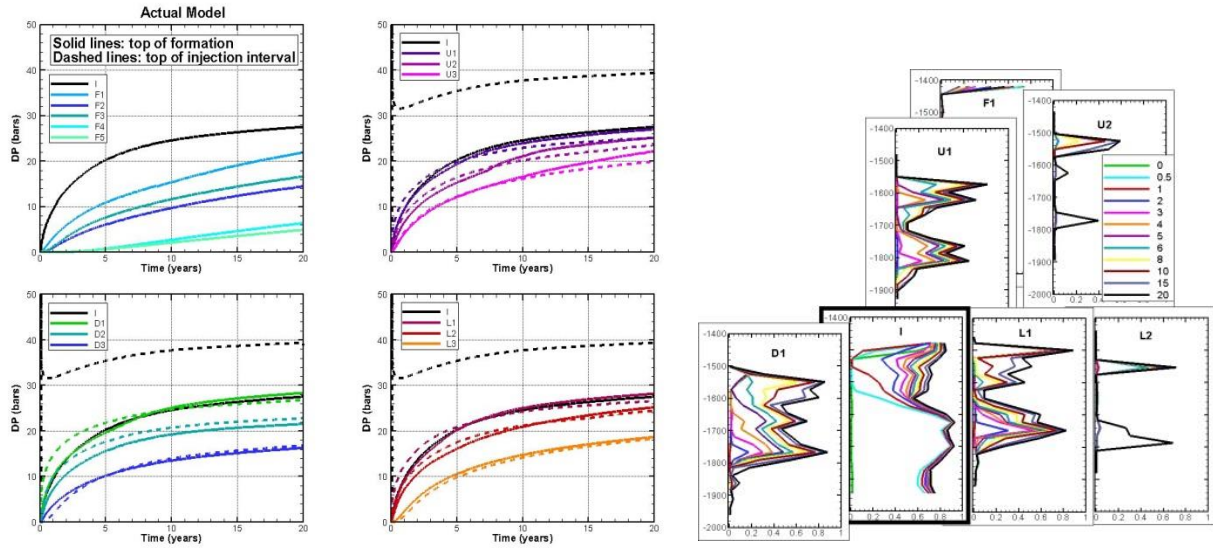


515
 516 *Figure 29. Ten-year operational model Year 10 hindcast: (a) pressure transients, (b) saturation*
 517 *profiles.*

518
519
520
521
522
523
524
525
526
527
528
529
530
531
532
533

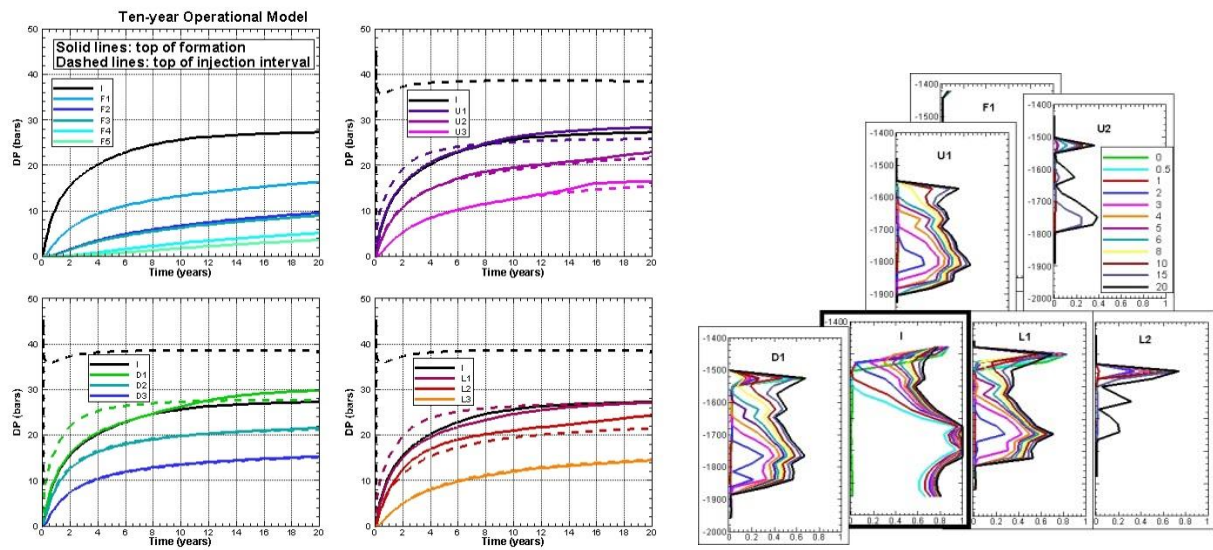
Year 20 – End of Injection Period

The actual model monitoring data for the 20th year are shown in Figure 30. At 20 years the injection well and six monitoring wells show saturation changes relative to initial conditions. The corresponding forecast results for the ten-year operational model run out to 20 years are shown in Figure 31. For the actual model all dP versus time curves are gradually increasing, but for the operational model they tend to increase too fast early, then level off too much late, showing too much curvature. This occurs more for the pressures at the depth of the perforated interval and is especially obvious at the injection well. However, the magnitude of dP is about right at 20 years. In an attempt to get more gradually increasing pressure curves, the two faults were extended farther updip, to create a more linear, less radial flow geometry. This is the only change made to create the final twenty-year operational model, and hindcast results are shown in Figure 32. The dP versus time curves show slightly less curvature. The saturation profiles for the ten-year and twenty-year operational models are very similar, and provide a reasonable concordance to the actual model.



534

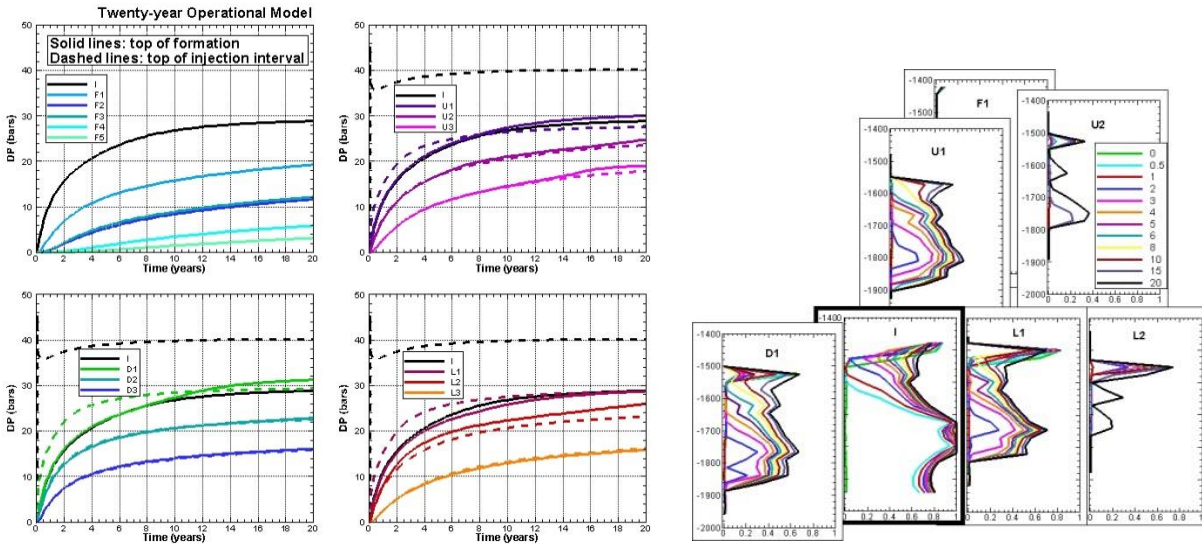
535 *Figure 30. Actual model Year 20 results: (a) pressure transients, (b) saturation profiles.*



536

537 *Figure 31. Ten-year operational model Year 20 forecast: (a) pressure transients, (b) saturation*
 538 *profiles.*

539



540

541 *Figure 32. Twenty-year operational model Year 20 hindcast: (a) pressure transients, (b)*
 542 *saturation profiles.*

543

544 **Year 25**

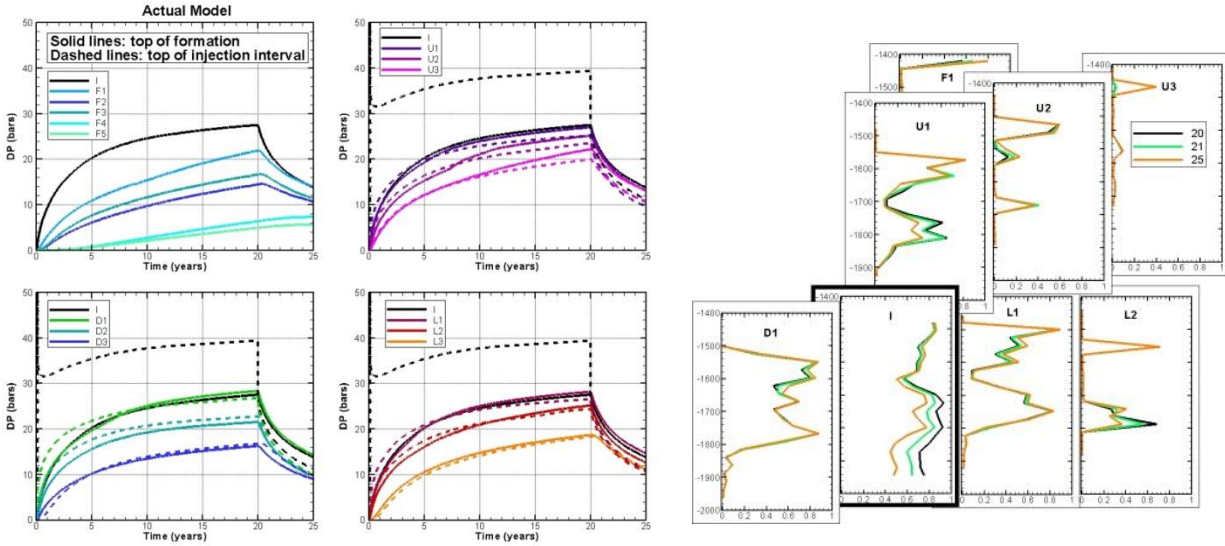
545 The actual model monitoring data for the 25th year are shown in Figure 33. This is the first
 546 observation within the post-injection period. For clarity, only saturation profiles from the post-
 547 injection period are shown. After injection ends at 20 years, pressure change is decreasing in all
 548 wells except the two most distant monitoring wells, F4 and F5, where it is still increasing slowly.

549 At 25 years the injection well and seven monitoring wells show saturation changes relative to
 550 initial conditions. Gas saturation is decreasing in the deeper portion of the formation and
 551 increasing in the shallow portion, as buoyancy flow acts to lift the CO₂ plume. The
 552 corresponding forecast results for the twenty-year operational model are shown in Figure 34.

553 This is a non-hysteretic model with $S_{gr} = 0$ during the injection period and $S_{gr} = 0.2$ during the
 554 post-injection period.

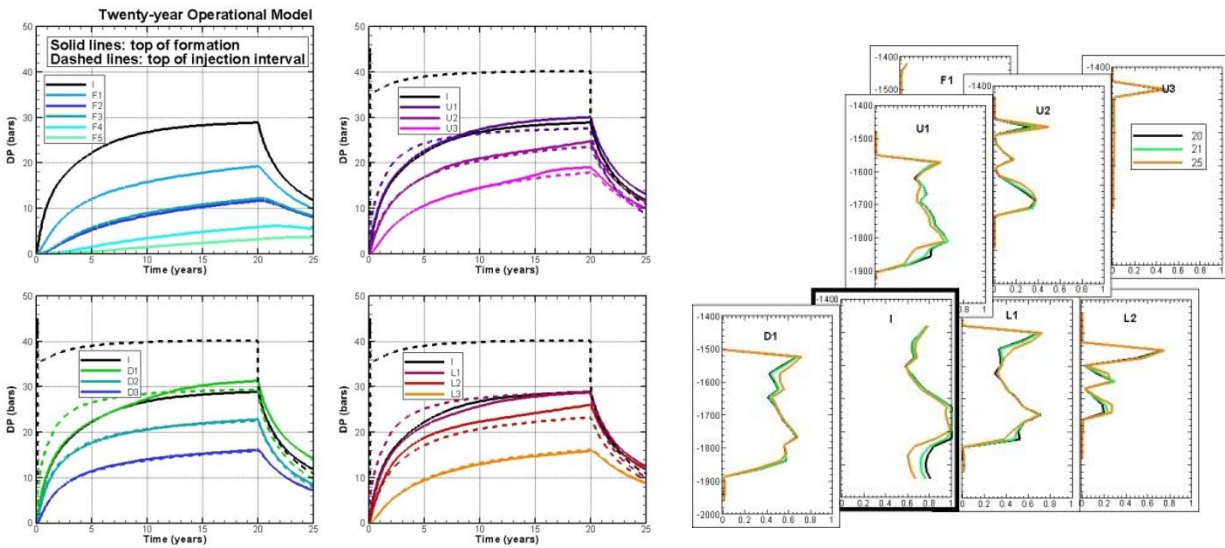
555 By the end of the injection period, most of the dP values for the twenty-year operational model
 556 are too big, and the curvature of the dP versus time curve indicates too rapid a response for all

557 wells, which is notable especially at the perforated interval of Well I, which flattens out too
558 much towards the end of the injection period, and the far wells F4 and F5, for which dP does not
559 continue to increase after injection ends. This suggests that the rock compressibility should be
560 larger, to provide a generally slower response. Comparing the post-injection saturation profiles
561 for the actual and twenty-year operational model shows that the gradual decline in gas saturation
562 over the lower half of the reservoir, which occurs as CO_2 moves upward under buoyancy forces
563 and water imbibes back into the pore space, is not produced by the operational model, indicating
564 that this non-hysteretic approximation with $S_{gr} = 0.2$ for the post-injection period overestimates
565 trapping of CO_2 . After several iterations, the final twenty-five year operational model has
566 doubled rock compressibility ($0.3\text{E-}8 \text{ Pa}^{-1}$ to $0.6\text{E-}8 \text{ Pa}^{-1}$), and two variations considered to better
567 represent imbibition: a non-hysteretic model with $S_{gr} = 0$ for the post-injection period and a
568 hysteretic model. The hysteretic model has a variable S_{gr} ; during the injection period it remains
569 zero nearly everywhere, and during the post-injection period it varies spatially and temporally
570 from zero to $S_{grmax} = 0.2$, depending on the maximum value of S_g experienced by a given
571 location. At the perforated interval, where the maximum S_g during the injection period was near
572 one, $S_{gr} \sim S_{grmax}$.



573

574 *Figure 33. Actual model Year 25 results: (a) pressure transients, (b) saturation profiles for the*
 575 *first five years of the post-injection period.*



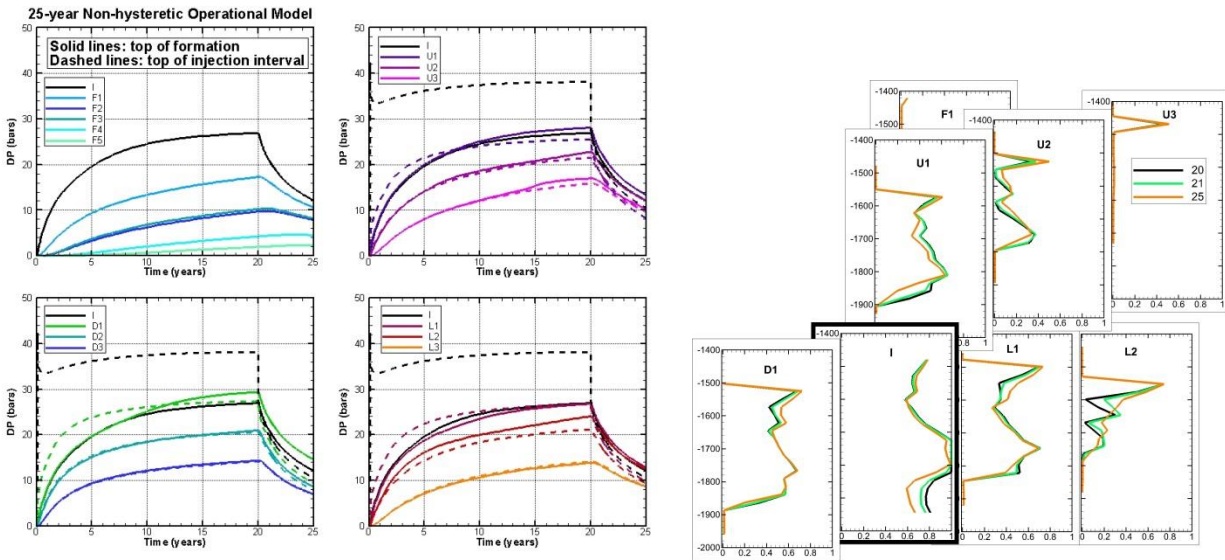
576

577 *Figure 34. Twenty-year operational model Year 25 forecast: (a) pressure transients, (b)*
 578 *saturation profiles for the first five years of the post-injection period. Non-hysteretic model with*
 579 *$S_{gr} = 0.2$ during post-injection period.*

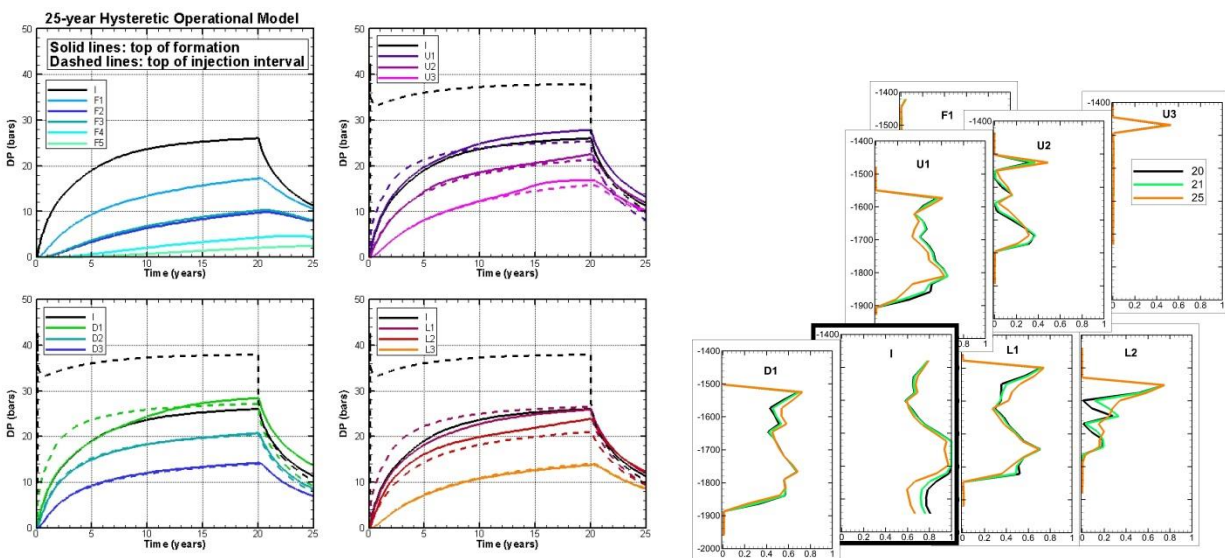
580

581 The hindcast results for the non-hysteretic twenty-five-year operational model (Figure 35) and
 582 hysteretic twenty-five-year operational model (Figure 36) show similar pressure transients and
 583 saturation profiles. Although the maximum pressure change at the end of injection is now

584 slightly small for most wells, the curvature of the dP versus time curve is a little better.
 585 Operational-model saturation profiles now match the character of the actual model much better,
 586 with gradual saturation decline in the lower half of the reservoir.



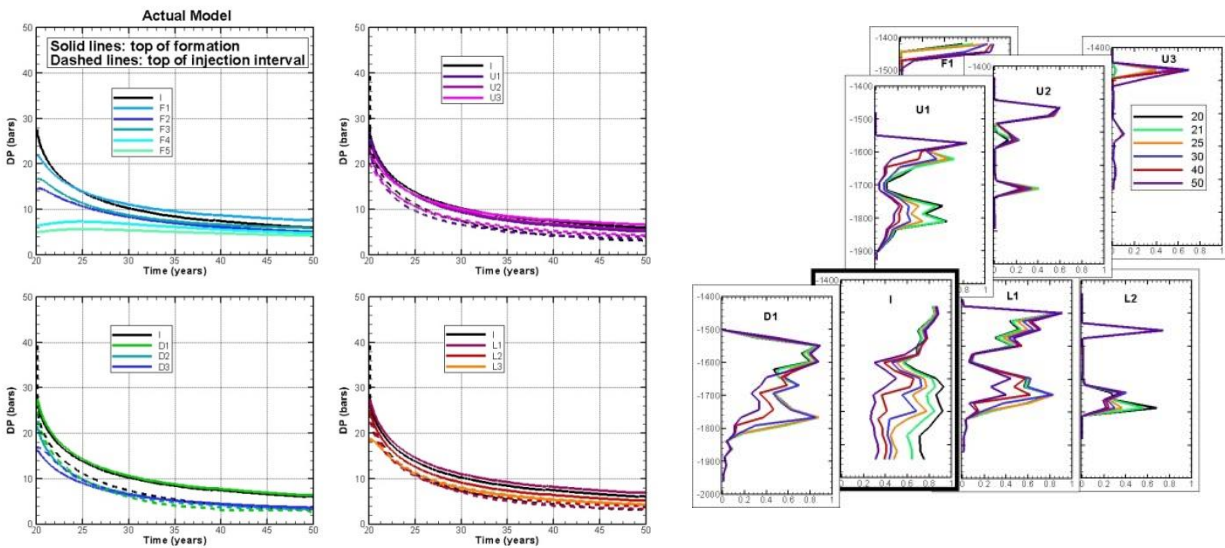
587
 588 *Figure 35. Twenty-five-year non-hysteretic model Year 25 hindcast: (a) pressure transients, (b)*
 589 *saturation profiles for the first five years of the post-injection period. Non-hysteretic model with*
 590 *$S_{gr} = 0$ during post-injection period.*



591
 592 *Figure 36. Twenty-five-year hysteretic model Year 25 hindcast: (a) pressure transients, (b)*
 593 *saturation profiles for the first five years of the post-injection period.*

594 **Year 50**

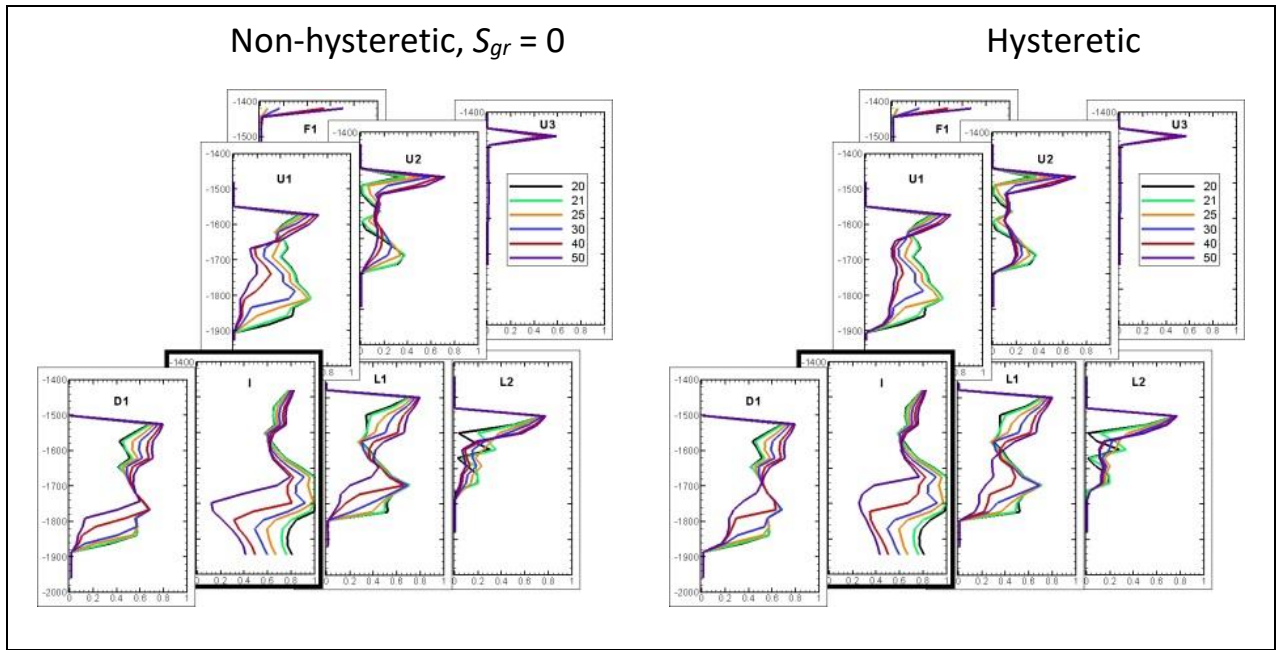
595 The actual model monitoring data for the 50th year are shown in Figure 37. At 50 years the
596 injection well and seven monitoring wells show saturation changes relative to initial conditions.
597 Pressure change is now decreasing in all wells. Gas saturation continues decreasing in the deeper
598 portion of the formation and increasing in the shallow portion, as buoyancy flow acts to lift the
599 CO₂ plume upward and updip in the storage formation. The corresponding forecast results for the
600 saturation profiles for the twenty-five-year operational models are shown in Figure 38. Pressure
601 transients for the operational models (not shown) are similar to those for the actual model.



602

603 *Figure 37. Actual model Year 50 results: (a) pressure transients, (b) saturation profiles for the*
604 *first 30 years of the post-injection period.*

605



606

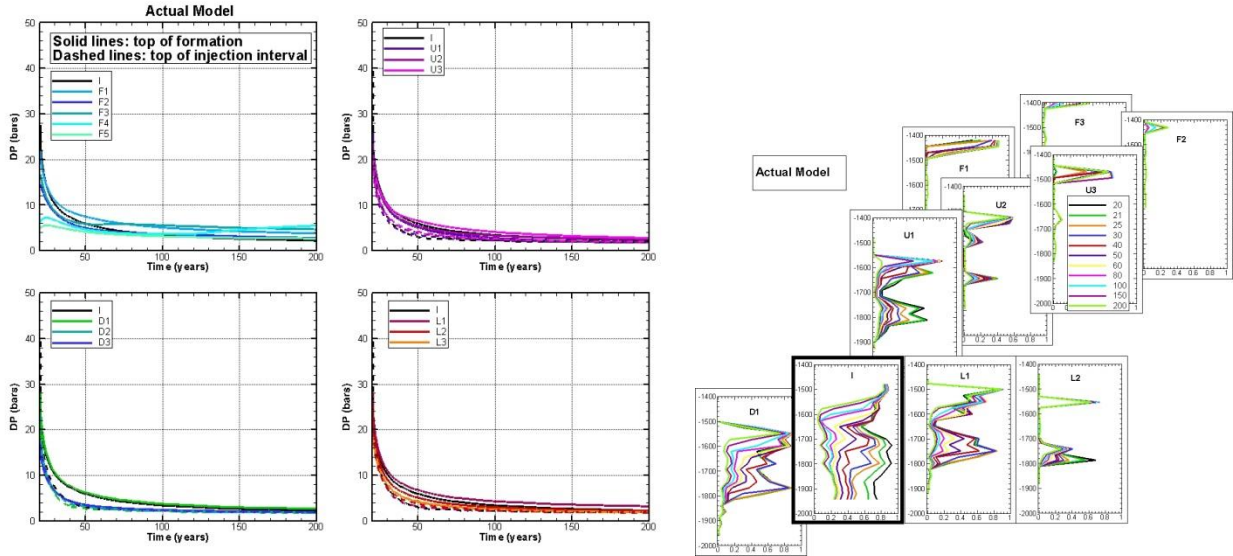
607 *Figure 38. Twenty-five-year operational models Year 50 forecast: saturation profiles for the first*
 608 *30 years of the post-injection period.*

609 Comparison of the late-time saturation profiles in Figure 38 indicates that as S_g decreases, the
 610 non-hysteretic model fails to show a convergence of S_g to 0.2 as the actual model (Figure 37) and
 611 hysteretic operational model do. Hence only the hysteretic model is used for continued
 612 operational model development.

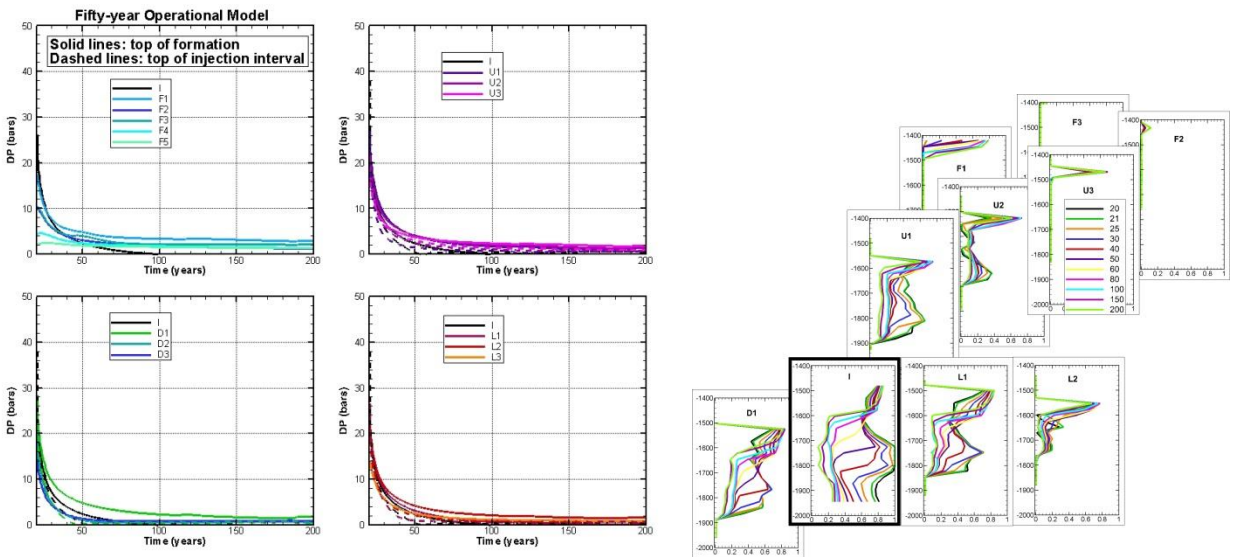
613 ***Years 100, 150, and 200***

614 The actual model monitoring data through the end of the PISC period at 70 years and on to 200
 615 years are shown in Figure 39. Starting at 100 years, the injection well and nine monitoring wells
 616 show saturation changes. The corresponding forecast results for the fifty-year operational model
 617 are shown in Figure 40. The gradual decline in the dP versus time curves is similar in both
 618 models, but the actual model dP curves tend to plateau above zero, whereas most of the
 619 operational model curves approach zero. Both models show the saturation continuing to decline
 620 in the lower half of the formation, but at a slowing rate, as saturations approach residual

621 saturation. The fifty-year operational model concordance to the actual data is deemed acceptable
 622 for 100, 150, and 200 years and no further model development is done.



623
 624 *Figure 39. Actual model pressure transients and saturation profiles for the entire post-injection*
 625 *simulation period.*



626
 627 *Figure 40. Fifty-year operational model pressure transients and saturation profiles for the entire*
 628 *post-injection simulation period.*

629 Table 2. Summary of development of operational models.

Year	Change in Saturation Profile*	Operational Model at Start of Year's Development	Observations from Operational Model		Changes Made to Operational Model	Number of Iterations
			Pressure transients	Saturation profiles		
1	I	Permeability 24 mD, no layering, no faults, no lateral heterogeneity, non-hysteretic relative permeability, no CH ₄	<i>dP</i> too big near I, too small far from I	<i>S_g</i> (<i>z</i>) too uniform at I	Increase permeability; introduce layering at perforated interval	6
2	I, L1, D1	Layering at perforated interval (3 - 121 mD), permeability 121 mD above perforated interval	<i>dP</i> at I perforated interval too big; <i>dP</i> at L3 too big	<i>S_g</i> peaks at L1 and D1 late arriving; <i>S_g</i> peak above perforated interval in I is missing	Modify permeability layering at perforated interval; introduce layering above perforated interval; Introduce fault between L2 and L3	3
3	I, L1, D1, U1	Layering at perforated interval (2 mD – 300 mD), layering above perforated interval (100 – 150 mD), L2/L3 fault permeability 5 mD	<i>dP</i> too big near I	<i>S_g</i> peaks okay, but too broad	Modify permeability layering; increase permeability at perforated interval, decrease permeability shallow	3
5	I, L1, D1, U1	Layering at perforated interval (4 mD – 600 mD), layering above perforated interval (50 – 150 mD), fault	Curvature of <i>P</i> vs <i>t</i> too large; <i>dP</i> at I perforated interval	<i>S_g</i> peaks okay, but too broad	Modify permeability layering: decrease permeability just above perforated interval; include	8

		permeability 15 mD	too small		CH ₄	
10	I, L1, L2, D1, U1, U2	Layering at perforated interval (4 mD – 600 mD), layering above perforated interval (25 – 141 mD), fault permeability 15 mD; CH ₄ included	dP generally too small; curvature unchanged	S_g peaks at perforated interval okay, shallow CO ₂ peaks too small	Modify permeability layering: decrease permeability at perforated interval and increase permeability shallow; Introduce fault west of well field; increase permeability of L2/L3 fault	6
20	I, L1, L2, D1, U1, U2, F1	Layering at perforated interval (3 mD – 400 mD), layering above perforated interval (50– 500 mD), L2/L3 fault permeability 30 mD; west fault permeability 1 mD; CH ₄ included	Curvature a little smaller, but still too large; dP generally okay at 20 years	S_g profiles generally good for both CO ₂ and CH ₄	Extend both faults farther updip	1
25	I, L1, L2, D1, U1, U2, U3, F1	Same as 20 years except faults extended in updip direction. Non-hysteretic model with $S_{gr} = 0.2$ during post-injection period	Curvature a little smaller	S_g profiles do not decrease enough from their maximum during early post-injection period	Double rock compressibility; eliminate non-hysteretic model with $S_{gr} = 0.2$ during post-injection period; develop non-hysteretic model with $S_{gr} = 0$ during post-injection period and hysteretic model with $S_{grmax} = 0.2$	3

50	I, L1, L2, D1, U1, U2, U3, F1	Same as 25 years except rock compressibility doubled to 0.6e-8; non-hysteretic model with $S_{gr} = 0$, hysteretic model with $S_{grmax} = 0.2$	Curvature a little smaller; dP still too small at far wells; no significant effect of hysteresis	Non-hysteretic model with $S_{gr} = 0$: S_g profiles decrease too much near $S_g = 0.2$	Eliminate non-hysteretic model with $S_{gr} = 0$	2
100	I, L1, L2, D1, U1, U2, U3, F1, F2, F3	Same as 50 years, but hysteretic model only	dP all approaching zero	S_g changes getting smaller		1

630 *Bold indicates the first time a well shows a saturation change

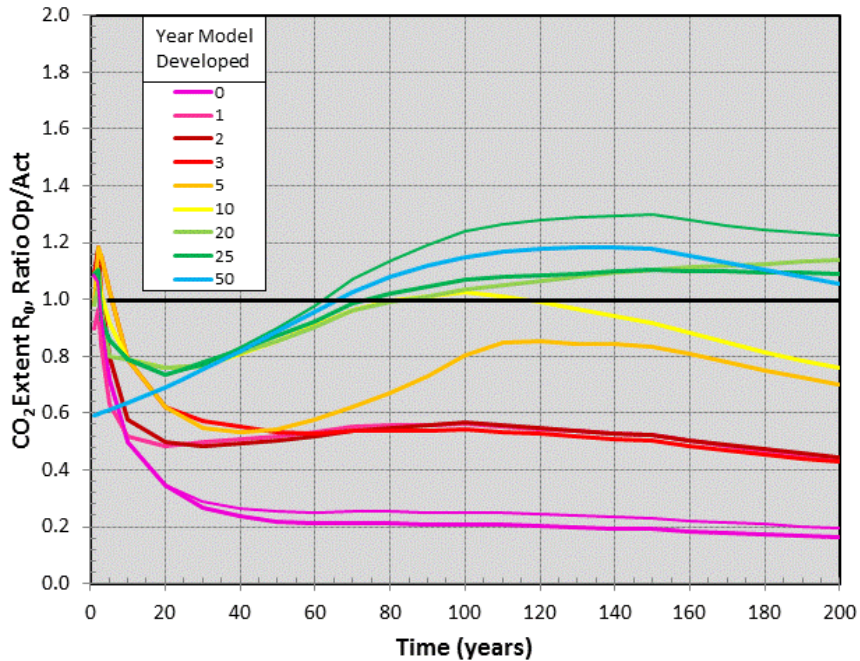
631 **Two Key Operational Model Metrics**

632 After each operational model shown in Table 2 was completed, it was used to simulate the entire
633 period from zero to 200 years. The two key metrics obtained from these simulations are the
634 radius of the CO₂ plume (R_0 , where S_g and CO₂ mass fraction are at least 0.02) as a function of
635 time, and the radius at which the pressure response is big enough to drive fluid through a
636 hypothetical flow path in the caprock (R_1 , where $dP \geq 1$ bar), which occurs at the end of the
637 injection period (20 years). These two key metrics also define Area of Review (AoR) under the
638 U.S. EPA Class VI well regulation (U.S. EPA, 2013).

639 Figure 41 plots the ratio of R_0 for the operational and actual models as a function of time for each
640 operational model. A ratio less than one indicates that the operational-model plume does not
641 migrate as far updip as the actual-model plume, and this is the result for all the early operational
642 models. Later operational models under-predict plume migration at early times, but slightly over-
643 predict it at later times. Two results are shown for the initial operational model (Year 0) and the
644 twenty-five-year operational model, both of which are non-hysteretic, one with $S_{gr} = 0$ during the

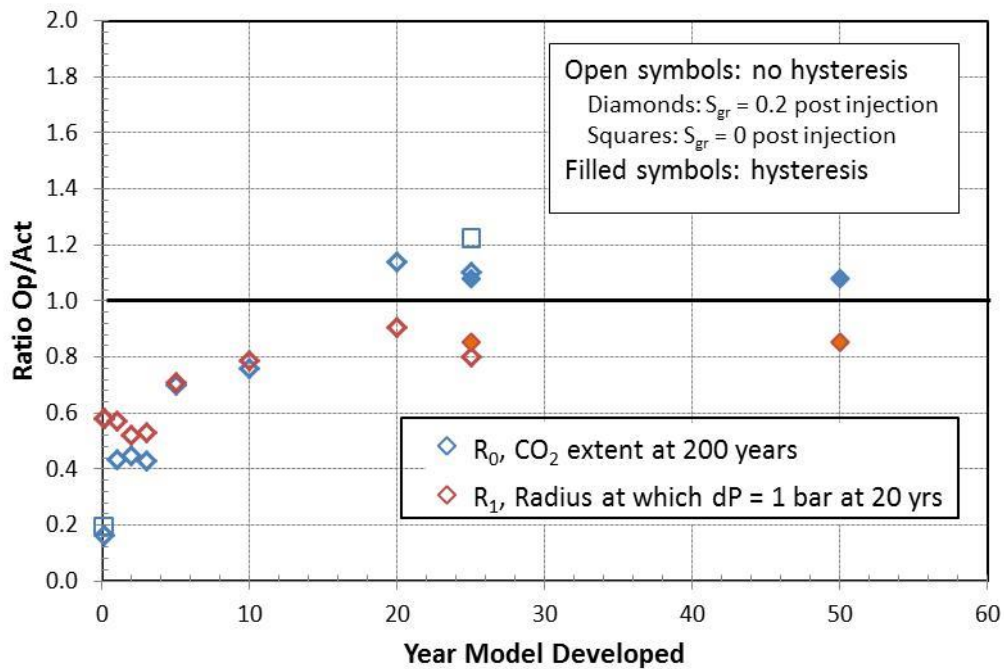
645 post-injection period, and the other with $S_{gr} = 0.2$. The fifty-year operational model is a
646 hysteretic model, with history-dependent S_{gr} , and as expected, its results are bracketed by the two
647 twenty-five-year non-hysteretic models. The large difference between the ratios for the twenty-
648 five-year non-hysteretic models (dark green curves) is one indication that using a hysteretic
649 model helps reduce uncertainty in plume-migration prediction. If one had used the difference
650 between the initial non-hysteretic models (pink curves) to judge the importance of including
651 hysteresis, the small difference would have been misleading because the updip migration of the
652 initial plume is so small (less than 20% of the actual migration) that there is little opportunity for
653 hysteretic effects to come into play.

654 Figure 42 plots the ratio of R_0 for the operational and actual models for 200 years, as a function
655 of the year the model was developed, illustrating the gradual decrease in uncertainty in CO₂
656 updip migration as more data are used to improve the operational model. Figure 42 also shows
657 the analogous plot for the pressure response R_1 for 20 years, again illustrating a gradually
658 decreasing trend in uncertainty. Generally, the trend in R_1 is similar to that for R_0 , showing that
659 uncertainty in CO₂ plume migration and pressure response behave comparably: the initial
660 operational model produces a poor prediction of actual model behavior, while using 1-3 years of
661 monitoring data improves operational model predictions somewhat, and using 5 years improves
662 them more, and by 10 years the operational model is significantly closer to the actual model.
663 Using data collected between 10 and 25 years further improves the operational model.



664

665 *Figure 41. Ratio of the updip CO₂ plume migration R₀ for operational (Op) and actual (Act)*
 666 *models, as a function of time. Values less than one indicate the operational model does not move*
 667 *as far updip as the actual model. The legend identifies the year the operational model was*
 668 *developed. For the 0- and 25-year operational models, the thinner line has S_{gr} = 0 and the*
 669 *thicker line has S_{gr} = 0.2.*



670

671 *Figure 42. Ratios of R₀ and R₁ for operational (Op) and actual (Act) models, with the horizontal*
 672 *axis indicating the year the operational-model was developed. Values of R₀ less than one*
 673 *indicate the operational-model CO₂ plume does not move as far updip as in the actual model.*

674

675 **5. Discussion**

676 The hypothesis investigated in this study is that uncertainties in forecasts of CO₂ plume evolution
677 and pressure change decrease over time as more operational data are collected and incorporated
678 into operational models. The key features of the pressure transients examined (and the model
679 properties they inform) are:

- 680 • magnitude of overall pressure change (horizontal permeability)
- 681 • difference between responses at monitoring wells that are near the injection well and
682 those that are farther away (horizontal permeability)
- 683 • difference between responses at the perforated interval and at the top of the formation
684 (vertical permeability)
- 685 • curvature of the dP versus time plots (flow field geometry, storativity).

686 An important point to note about the saturation profiles is that for the operational model profiles
687 tend to show saturation peaks at the same depths, because the operational model is layered,
688 whereas the actual model shows saturation peaks at different depths, because the lateral and
689 vertical heterogeneity enables irregular fluid flow paths upward and updip through the formation
690 under buoyancy forces. Thus rather than comparing the exact depth of saturation peaks, we try to
691 match the general trend of peaks developing first at the perforated interval near the injection
692 well, and moving gradually upward and updip, which is sensitive to both horizontal and vertical
693 permeability.

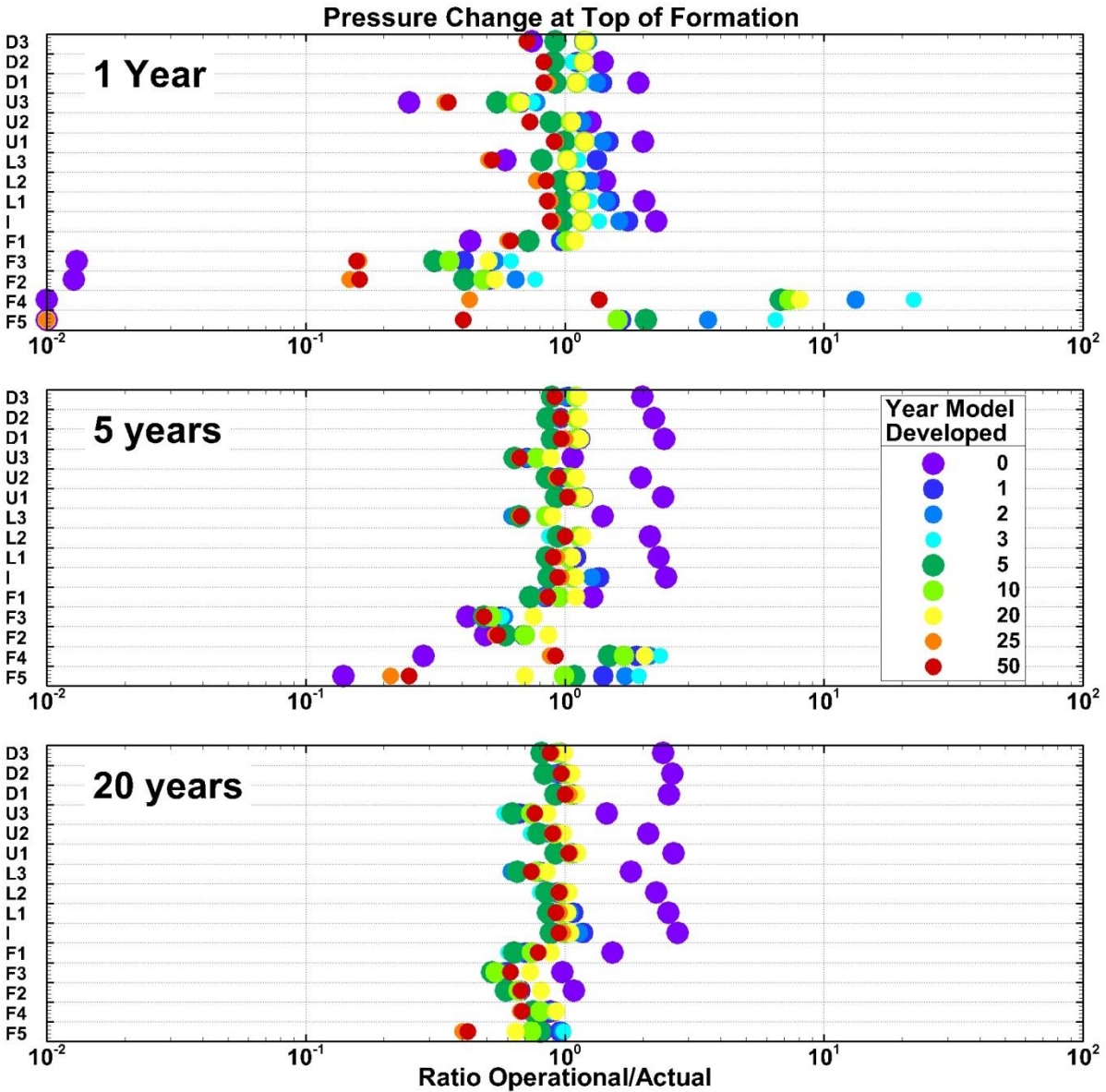
694 We present in Figures 43 and 44 a compact summary of the evolution of uncertainty of these key
695 measures of GCS system changes. The plots show concordance at selected monitoring locations
696 at three different times through the plotting of pressure change and gas saturation for the series of
697 operational models developed over time (different colored circles) normalized by the actual
698 values at those same locations and times. For example, the purple circle labeled with a zero
699 would be the initial model (model developed at year zero) and the corresponding normalized
700 results from that initial model are shown at 1 year, 5 years, and 20 years. Similarly, the dark
701 blue, medium blue, light blue etc. circles represent the years 1, 2, 3, etc., respectively, that the
702 model was updated. For pressure change, results at times during the CO₂ injection period are
703 most relevant, whereas for gas saturation, results at later times (e.g., post-injection times when
704 the CO₂ plume has reached many monitoring wells) are of more interest. Figure 43 shows that
705 despite some scatter, there is a general trend of migration of the forecasted pressure differences
706 in the figure toward the line where operational normalized by actual equals unity. Figure 44
707 shows analogous results for saturation in the top layer at three different times. The trend toward
708 better concordance (reduced uncertainty) over time is not as clear for the saturation as for
709 pressure because saturation is much more sensitive to local permeability heterogeneity in the
710 model. Nevertheless, there is improvement over time at many locations, and this result mimics
711 what would actually be observed in field data that are limited and subject to vagaries of
712 measurement location in a heterogeneous natural system. Overall, Figures 43 and 44 make the
713 point that uncertainty in the plume's future migration and effects on the subsurface are large at
714 the beginning, but with competent monitoring and updating of operational models, the
715 uncertainty trends downward over time.

716 Some details of the particular system we studied may be useful for cases of GCS in depleted
717 natural gas reservoirs. For example, we observed that when both CH₄ and CO₂ are included in
718 the model, distant monitoring wells show a distinctive signal of a CH₄ arrival presaging the CO₂
719 arrival. This effect has been observed and modeled previously (e.g., Oldenburg et al., 2013). We
720 also found that the decline of saturation peaks in the post-injection period requires imbibition and
721 capillary trapping to be properly modeled

722 Table 2 shows the year when the CO₂ plume reaches each monitoring well, indicating that for the
723 first three years, CO₂ reaches only the nearest three wells (D1, L1, and U1). The CO₂ plume
724 reaches only five wells during the first 10 years of injection, and only six wells by the end of the
725 injection period at 20 years. This sequence suggests the idea of initially drilling only a few
726 monitoring wells near the injection well, then adding more monitoring wells as the CO₂ plume
727 grows. Adding one or two new monitoring wells every 5-10 years, with locations informed by
728 previous plume development, should be a cost-effective approach to monitoring CO₂ plume
729 migration. In contrast, the pressure-transient information provided by distant wells is useful
730 even at early times. Thus, a good initial monitoring well configuration might consist of three
731 nearby wells (e.g., D1, L1, U1), and one or two more distant well (e.g., F3, F4). Another
732 possibility for minimizing the number of monitoring wells would be to augment monitoring-well
733 observations with time-lapse geophysical surveys (e.g., Doughty and MacLennan, 2018; Pevzner
734 et al., 2011; Daley et al., 2011).

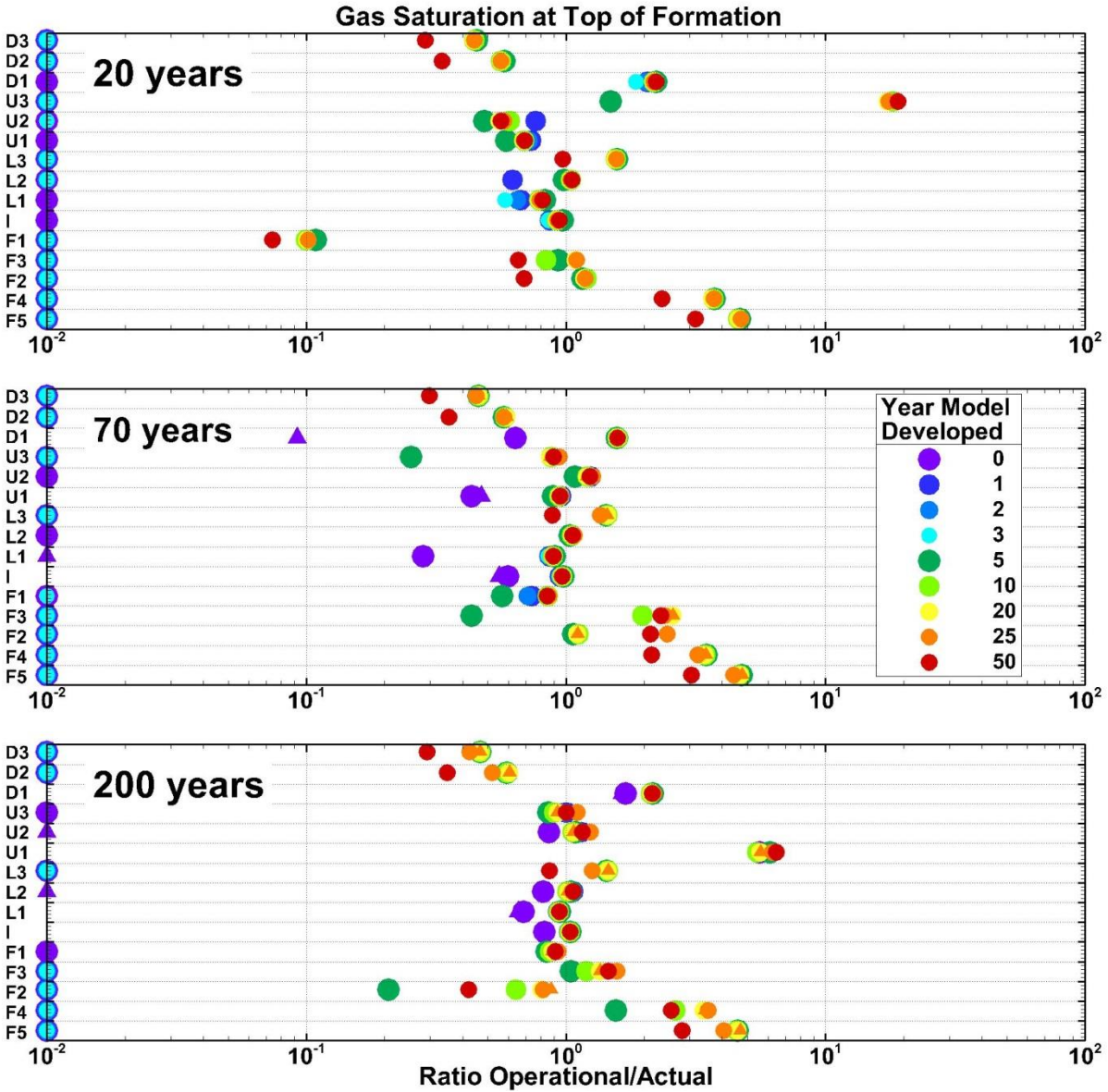
735 Perfect concordance between operational and actual model pressure transients and saturation
736 profiles is not expected given the significant lateral heterogeneity of the actual model (e.g.,
737 Figures 3 and 6) which is not included in the operational models. Of course, pressure-transient
738 data from multiple wells can be inverted to estimate heterogeneous permeability distributions,

739 but with pressure data from only two depths (the top of the perforated interval and the top of the
740 storage formation), and local permeability values required for more than 20 model layers, this
741 would be an ill-posed inverse problem, requiring sophisticated inverse methods. Doing a joint
742 inversion of pressure-transient and saturation profile data is also a possibility, but again would
743 require advanced inverse methods. Such approaches are not in keeping with our conceptual
744 model of field operators using and updating (improving) relatively simple numerical models.
745 Instead, we acknowledge that concordance will not be perfect, and try to improve the model by
746 looking at general trends in the pressure transients and saturation profiles, as described in the
747 previous section, just as operators are expected to do.



748

749 *Figure 43. Ratio of pressure change (operational/actual) at three times for each monitoring well*
 750 *for the sequence of operational models (color identifies the year the model was developed),*
 751 *showing general evolution toward the line where operational/actual equals one. For the 0- and*
 752 *25-year non-hysteretic models, two values of residual gas saturation are shown: circles indicate*
 753 *$S_{gr} = 0$ and deltas indicate $S_{gr} = 0.2$. Symbols are slightly different sizes for better visibility of*
 754 *tightly grouped symbols.*



755

756 *Figure 44. Ratio of saturation at top of storage formation (operational/actual) at three times for*
 757 *each monitoring well, for the sequence of operational models (color identifies the year the model*
 758 *was developed), showing general evolution toward the line where operational/actual equals one.*
 759 *For the non-hysteretic models, two values of residual gas saturation are shown: circles indicate*
 760 *$S_{gr} = 0$ and deltas indicate $S_{gr} = 0.2$. Symbols are slightly different sizes for better visibility of*
 761 *tightly grouped symbols.*

762

763 **6. Conclusions**

764 We have illustrated the year-by-year improvement to an initially simple operational model of
765 CO₂ sequestration in a depleted natural gas reservoir. The analysis of each year's pressure-
766 transient and saturation-profile data provides the impetus for modifications to the operational
767 model. Two key metrics represent the ability of the operational model to accurately predict the
768 results of the actual model: the extent of the CO₂ plume updip migration, and the radial extent of
769 the pressure pulse. Deviations between the actual and operational models for both of these
770 metrics steadily decrease as more monitoring data become available over time to improve the
771 operational model. While the goal of this paper was to show the reduction in uncertainty that
772 occurs when models are updated and improved based on operational data, the process by which
773 we demonstrated this reduction in uncertainty also illustrates a workflow that may a useful
774 example for site operators.

775 The summary plots (Figures 41 – 44) indicate that for a twenty-year injection period, using
776 monitoring data for the first 10 years greatly improves the ability of the operational model to
777 predict the 50-year PISC period and out to the end of the entire 200 year simulation. In fact, data
778 from the first year are already valuable, especially in constraining near-injection-well properties.
779 However, including data from the post-injection period is mandatory for understanding both the
780 drainage and imbibition aspects of CO₂ plume migration, and for the present example with a
781 high-permeability storage formation and significant updip CO₂ migration, it was necessary to use
782 a hysteretic model to properly account for both of these processes. Some of the parameters of the
783 hysteretic model could be inferred from just the first five years of the post-injection period, when
784 the saturation peaks first began to decrease, but a clearer picture emerged by considering longer
785 post-injection times around 50 years, when saturation values neared the residual saturation.

786 **Acknowledgements and Disclaimer**

787 We thank Jeff Wagoner of Lawrence Livermore National Laboratory for providing the geologic
788 model of the Southern Sacramento River Delta region, and Diana Bacon (PNNL) and
789 Christopher Brown (PNNL) for constructive reviews of an earlier draft. This work was supported
790 by the Assistant Secretary for Fossil Energy, Office of Sequestration, Hydrogen, and Clean Coal
791 Fuels, for the National Risk Assessment Partnership (NRAP) project managed by the National
792 Energy Technology Laboratory (NETL). Additional support came from the U.S. Department of
793 Energy under Contract No. DE-AC02-05CH11231. This report was prepared as an account of
794 work sponsored by an agency of the United States Government.

795 **References**

- 796 Burton, E., Mateer, N., Myhre, R., and Stone, M., 2016. WESTCARB Phase III Final Report,
797 Summary of California Activities California Energy Commission Report CEC-500-2016-053, 49
798 pp.
799
800 California Air Resources Board, 2017. Carbon Capture and Sequestration Protocol
801 under the Low Carbon Fuel Standard.
802 https://www.arb.ca.gov/fuels/lcfs/ccs_protocol_010919.pdf
803
804 Chadwick, R.A. and Noy, D.J., 2015. Underground CO₂ storage: demonstrating regulatory
805 conformance by convergence of history-matched modeled and observed CO₂ plume behavior
806 using Sleipner time-lapse seismics. *Greenhouse Gases: Science and Technology*, 5(3), pp.305-
807 322.
808
809 Chen, Y. and Zhang, D., 2006. Data assimilation for transient flow in geologic formations via
810 ensemble Kalman filter. *Advances in Water Resources*, 29(8), pp.1107-1122.
811
812 Daley, T.M., Ajo-Franklin, J.B. and Doughty, C., 2011. Constraining the reservoir model of an
813 injected CO₂ plume with crosswell CASSM at the Frio-II brine pilot. *International Journal of*
814 *Greenhouse Gas Control*, 5(4), pp.1022-1030.
815
816 Deutsch, C.V. and Journel, A.G., 1992. *Geostatistical Software Library and User's Guide* (2nd
817 Ed.). Oxford University Press, New York.
818
819 Foxall, W., Doughty, C., Lee, K.J., Nakagawa, S., Daley, T., Burton, E., Layland-Bachmann, C.,
820 Borglin, S., Freeman, K., Ajo-Franklin, J., Jordan, P., Kneafsey, T., Oldenburg, C., Ulrich, C.,

821 2017. Investigation of Potential Induced Seismicity Related to Geologic Carbon Dioxide
822 Sequestration in California, California Energy Commission Report CEC-500-2017-028.
823

824 Freifeld, B.M., Trautz, R.C., Kharaka, Y.K., Phelps, T.J., Myer, L.R., Hovorka, S.D. and Collins,
825 D.J., 2005. The U-tube: A novel system for acquiring borehole fluid samples from a deep
826 geologic CO₂ sequestration experiment. *Journal of Geophysical Research: Solid Earth*,
827 *110*(B10).
828

829 Harp, D.R., Oldenburg, C.M. and Pawar, R., 2019. A metric for evaluating conformance
830 robustness during geologic CO₂ sequestration operations. *International Journal of Greenhouse*
831 *Gas Control*, 85, pp.100-108.
832

833 Keating, E.H., Doherty, J., Vrugt, J.A. and Kang, Q., 2010. Optimization and uncertainty
834 assessment of strongly nonlinear groundwater models with high parameter dimensionality. *Water*
835 *Resources Research*, *46*(10), W10517.
836

837 Le Guéan, T., Gravaud, I., De Dios, C., Gavilanes, L., Poletto, F., Eguilior, S. and Hurtado, A.,
838 2018, October. Determining performance indicators for linking monitoring results and risk
839 assessment—application to the CO₂ storage pilot of Hontomin, Spain. In *The Greenhouse Gas*
840 *Control Technologies-GHGT-14*.
841

842 Doughty, C. and MacLennan, K., 2018. Using TOGA to model CO₂-EOR in conjunction with
843 time-lapse electromagnetic monitoring, TOUGH Symposium 2018, Lawrence Berkeley National
844 Lab., Berkeley CA, October 8-10.
845

846 Oladyshkin, S., Class, H., Helmig, R. and Nowak, W., 2011. A concept for data-driven
847 uncertainty quantification and its application to carbon dioxide storage in geological formations.
848 *Advances in Water Resources*, *34*(11), pp.1508-1518.
849

850 Oldenburg, C.M., 2018. Are we all in concordance with the meaning of the word conformance,
851 and is our definition in conformity with standard definitions? *Greenhouse Gases: Science and*
852 *Technology*, 8(2), pp.210-214.
853

854 Oldenburg, C.M., Doughty, C. and Spycher, N., 2013. The role of CO₂ in CH₄ exsolution from
855 deep brine: Implications for geologic carbon sequestration. *Greenhouse Gases: Science and*
856 *Technology*, 3(5), pp.359-377.
857

858 Oldenburg, C.M., Pruess, K. and Benson, S.M., 2001. Process modeling of CO₂ injection into
859 natural gas reservoirs for carbon sequestration and enhanced gas recovery. *Energy & Fuels*,
860 *15*(2), pp.293-298.
861

862 Pevzner, R., Shulakova, V., Kepic, A. and Urosevic, M., 2011. Repeatability analysis of land
863 time-lapse seismic data: CO₂CRC Otway pilot project case study. *Geophysical Prospecting*,
864 *59*(1), pp.66-77.
865

- 866 Sun, A.Y., Morris, A.P. and Mohanty, S., 2009. Sequential updating of multimodal
867 hydrogeologic parameter fields using localization and clustering techniques. *Water Resources*
868 *Research*, 45(7), W07424.
- 869
870 U.S. EPA (United States Environmental Protection Agency), 2008. Federal Requirements under
871 the Underground Injection Control (UIC) Program for Carbon Dioxide (CO₂) Geologic
872 Sequestration (GS) Wells, Proposed Rule, 40 CFR Parts 144 and 146, EPA-HQ-OW-2008-0390.
873
- 874 U.S. EPA, Geologic Sequestration of Carbon Dioxide Underground Injection Control (UIC)
875 Program Class VI Well Area of Review Evaluation and Corrective Action Guidance Office of
876 Water (4606M), EPA 816-R-13-005, May 2013.
- 877 van Genuchten, M.Th., 1980. A closed-form equation for predicting the hydraulic conductivity
878 of unsaturated soils. *Soil Science Society of America Journal*, 44(5), pp. 892-898.
879
- 880 Walter, L., Binning, P.J., Oladyshkin, S., Flemisch, B. and Class, H., 2012. Brine migration
881 resulting from CO₂ injection into saline aquifers—An approach to risk estimation including
882 various levels of uncertainty. *International Journal of Greenhouse Gas Control*, 9, pp.495-506.